Design and Test of a Slab Waveguide Spectrometer for Spatial Heterodyne Observations of Water Vapor

Kenneth Sinclair

A thesis submitted to
the Faculty of Graduate Studies
in partial fulfillment of the requirements
for the degree of
Master of Science

Graduate program in Earth and Space Science
York University
Toronto, Ontario

April 2014

ABSTRACT

The Slab Waveguide Interferometric Spatial Heterodyne (SWISH) Spectrometer was designed as a high-resolution instrument designed to demonstrate the ability of slab waveguide spatial heterodyne spectrometer technology through measurements of water vapor in Earth's atmosphere. It is based on a multiaperture Fourier-transform planar waveguide spectrometer. The Fourier technique was used for spectra retrieval. The absorption signal will be measured with a spectral range of 2.5 nm centered in the near infrared spectral region on the 1.3645 μm wavelength with a spectral resolution of 0.05 nm. The resolution of the interferometer array is designed so that errors in the retrieved spectrum, measured using the least squares method, are minimized. The slab waveguide itself was constructed such that the interferometers and monitoring waveguides have an output pitch, which matches that of the linear detector array. It was designed for the 1.3645 μm wavelength range using a 1.3 μm wide and 0.75 μm high silicon-on-insulator (SOI) ridge waveguides and contained 100 Mach-Zehnder interferometers along with 11 'pass-through' waveguide.

This thesis spans several components of the project relating to the development and testing of the SWISH Spectrometer. These parts include: (1) developing and building a prototype slab waveguide spatial heterodyne spectrometer (SWSHS) chip and breadboard optical instrument at spatial heterodyne observations of water (SHOW) wavelengths; (2) investigating alternative method(s) for increased coupling efficiency; (3) assembling a prototype spectrometer for SHOW waveband; (4) assembling input optics for the SWSHS; (5) developing system packaging and build a prototype system; (6) developing inversion algorithms and calibration procedures for system using test data from laboratory tests of micro-SHOW linear prototype.

ACKNOWLEDEMENTS

Many people were involved to help make this project possible, and I am very grateful for their expertise and guidance. I am especially grateful for my wonderful mentors, Brian Solheim, Brendan Quine and Al Scott, who have provided me support and practical advice. I am also grateful to Mirek Florjańczyk at the National Research Council for his support and guidance over the years. I would also like to thank Stephen Brown at CRESS for his help in understanding issues and providing feedback. Finally, I have great thanks and appreciation for my wonderful, loving and supportive friends and family.

TABLE OF CONTENTS

LIST OF FIGURES

LIST OF TABLES

LIST OF EQUATIONS

1. PROJECT OVERVIEW

1.1 Introduction

1.1.1 Project Overview

York University's Center for Research in Earth and Space Science (CRESS) has worked in collaboration with the National Research Council of Canada (NRC) as well as COM DEV Canada Ltd. for several years on the development of slab waveguide technology. Three generations of slab waveguides were designed and fabricated. Results shown here are for the 3rd and most recent version, unless otherwise stated.

The most recent phase of the collaborative work resulted from the Canadian Space Agency's (CSA) Project Number 50142. The project had several goals relating to the development of Slab Waveguide technology, including building a prototype SWSHS chip and breadboard optical instrument at SHOW wavelengths, designing input coupling gratings, a feasibility study for long wave SHS (8-12 microns) and an investigation for alternative methods to increase coupling efficiency and building a prototype spectrometer for SHOW waveband. The NRC is responsible for developing a slab waveguide spectrometer using a spectral band appropriate to make measurements of water vapor. COM DEV is responsible for designing and building the housing of the instrument. Lastly, the instrument was given to CRESS after assembly and calibration.

I have been involved in the development of slab waveguide technology for several years, initially working with the CRESS and the National Research Council to develop retrieval algorithms as a summer research assistant. Working with each of the parties, the NRC, COM DEV and CRESS,

throughout the entire development of this spectrometer allowed me to be involved in several aspects of this project relating to the development and testing of the Slab Waveguide Interferometric Spatial Heterodyne (SWISH) Spectrometer.

1.1.2 Spectrometer Overview

The SWISH Spectrometer (Florjańczyk et al., 2007) is a high-resolution instrument designed to demonstrate the ability of slab waveguide spatial heterodyne spectrometer technology through measurements of water vapor in Earth's atmosphere (Florjańczyk et al., 2009). It is based on a multiaperture Fourier-transform planar waveguide spectrometer. The Fourier technique is used for spectra retrieval. The absorption signal will be measured with a spectral range of 2.5 nm centered in the near infrared spectral region on the 1.3645 μm wavelength with a spectral resolution of 0.05 nm (Florjańczyk et. al., 2011). The resolution of the interferometer array is designed so that errors in the retrieved spectrum, measured using the least squares method, are minimized. Measurements will be made in a solar occultation configuration from an airborne platform (Scott et al., 2009).

Using a 1° field of view for a solar occultation technique, the SWISH spectrometer combines large throughput (étendue) with high spectral resolution and high vertical resolution to make measurements of water vapour in Earth's atmosphere from the high troposphere to the mesosphere. The functional requirements of the spectrometer include a vertical atmospheric resolution of less than 1 km and a horizontal resolution of less than 300 km.

The slab waveguide itself was constructed such that the interferometers and monitoring waveguides have an output pitch, which matches that of the linear detector array (Florjańczyk et al., 2008). It was designed for the 1.3645 μm wavelength range using a 1.3 μm wide and 0.75 μm high silicon-on-insulator (SOI) ridge and contained 100 Mach-Zehnder interferometers along with 11 'pass-through' waveguides (Florjańczyk et al., 2009). Each interferometer had a dual output, from an MMI coupler, which provided a discrete Fourier interferogram of incoming light onto 221 contiguous pixels of a Sensors Unlimited SU256LSB-1.7T1 InGaAs linear detector. The slab waveguide had a theoretical wavelength resolution of 0.05 nm and spectral range of 2.5 nm. The slab waveguide used previously is shown on the left in **Figure 1** and measures 24 by 15.6 mm while the chip designed for the SHOW waveband used in this phase of the development measures 57 by 32.5 mm and is shown on the right in **Figure 1**.

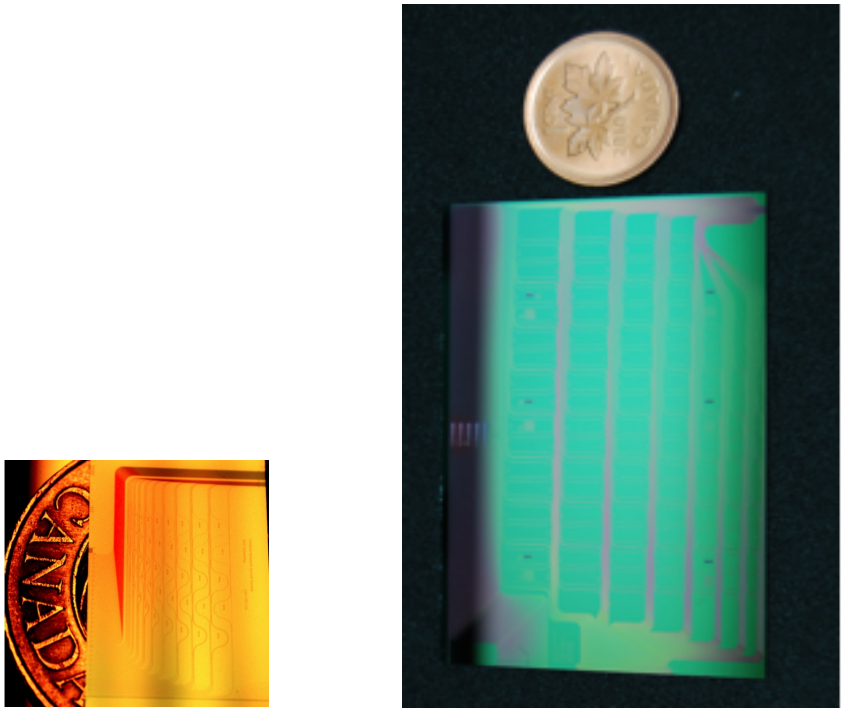

Figure 1: First generation waveguide (left) and second generation (right) (scale is approximate)

Slab waveguide spatial heterodyne spectrometers have been described in detail (Florjańczyk et. al., 2007; 2008; 2009). The interferometric technique requires no moving parts and combines large throughput (étendue) with high spectral resolution. It is based on the spatial heterodyne spectrometer (SHS) introduced by Harlander et al. (1992) in combination with recent advances in optical waveguide concepts developed over recent years for the telecommunications industry (Cheben et. al., 2007). This technology has mechanical robustness, high-throughput and low mass, which makes it suitable and attractive for space applications. The spectrometer can be compared to a bulk optics version (Lin et. al., 2004) having the same resolution and waveband of interest. They differ with the slab waveguide existing on a small piece of silicon, whereas the bulk optics use large pieces of glass.

The bulk optics also requires an arm length of 115 mm which adds to the volume requirements of the instrument.

1.1.3 Spectral Band of Interest

The band of interest is 2.5 nm wide and was chosen to isolate water vapor absorption. This is shown in **Figure 2** below. The instrument will use the near infrared region of the spectrum to isolate water vapor absorption signal.

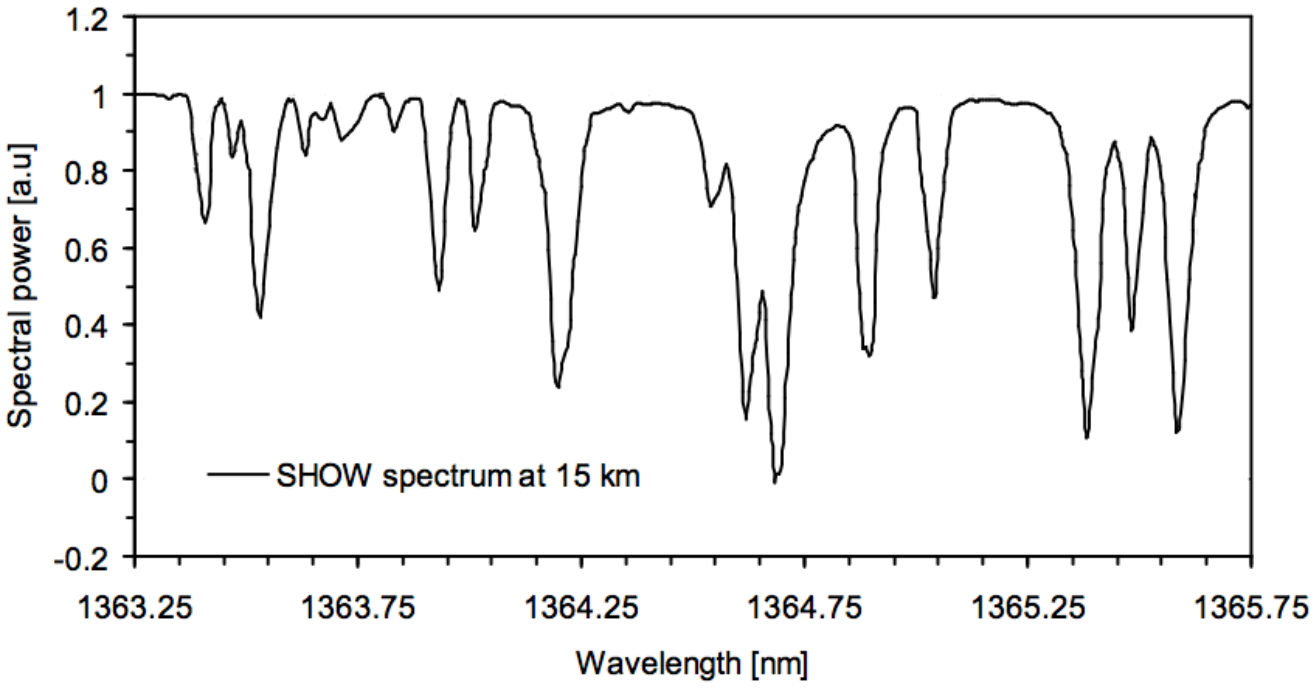

Figure 2: Transmission spectra of water vapor at 15 km altitude (solid line).

1.1.4 Merit of Project

Science

Water vapor is a key climate variable and the most significant greenhouse gas since it exerts the largest heat trapping effect of all atmospheric constituents and is also the most plentiful greenhouse gas (Pachauri & Reisinger, 2007). Water vapor changes represent the largest feedback as global average temperatures increase (Forster et al., 2007). Between 2003 and 2008 the global surface temperature varied by 0.6°C (Desslet et al., 2008). It contributes to the infrared opacity of the troposphere accounting for 60% of the natural greenhouse warming process through amplification of anthropogenic contribution. Water vapor accounts for the largest positive feedback in the climate system. However, it is not directly output to the atmosphere in significant quantities but has the feedback of increasing concentration within the atmosphere increases as the air temperature increases. This is due to warm airs capability of being able to hold more water vapor and its concentration can increase through evaporation. According to the intergovernmental panel on climate change, the positive feedback of water vapor can result in an increase in temperature equal to 60% of the change due to a doubling of carbon dioxide. The Union of Concerned Scientists state *the Role of Water Vapor and Clouds* as the first area for further research essential to refining computer models and reducing uncertainties about the future of climate. Achieving this goal will require observations of sufficient quality to discern water vapor concentrations and the true state of the water in the atmosphere. Improvements in measurements will be necessary, both temporally and spatially, in order to capture trends in behavior and characterize fundamental signatures of processes that are critical for evaluating and improving the predictive ability and realism of models.

Low Troposphere

In the lower troposphere, information has been available since 1979 and shows a strong interannual variability with observed long term increasing and decreasing trends depending on geographical region. Trenberth et al. (2005a) noted that the linear trends can be reproduced from observed sea surface temperatures (SSTs) changes during the same period.

Upper-Troposphere

In the upper-troposphere, water vapor accounts for a large part of the atmospheric greenhouse effect. Satellite data have shown a linear trend in relative humidity close to a +1% per decade. This is shown in **Figure 3** (right).

Stratospheric

Stratospheric water vapor has shown increases of 1% per year during the second half of the 20th century. Continuous and more reliable measurements have confirmed an increase during the 1980's and 1990's, however due to a lack of geographical coverage and high variability, the effect of stratospheric water vapor remains uncertain (Trenberth et al., 2007).

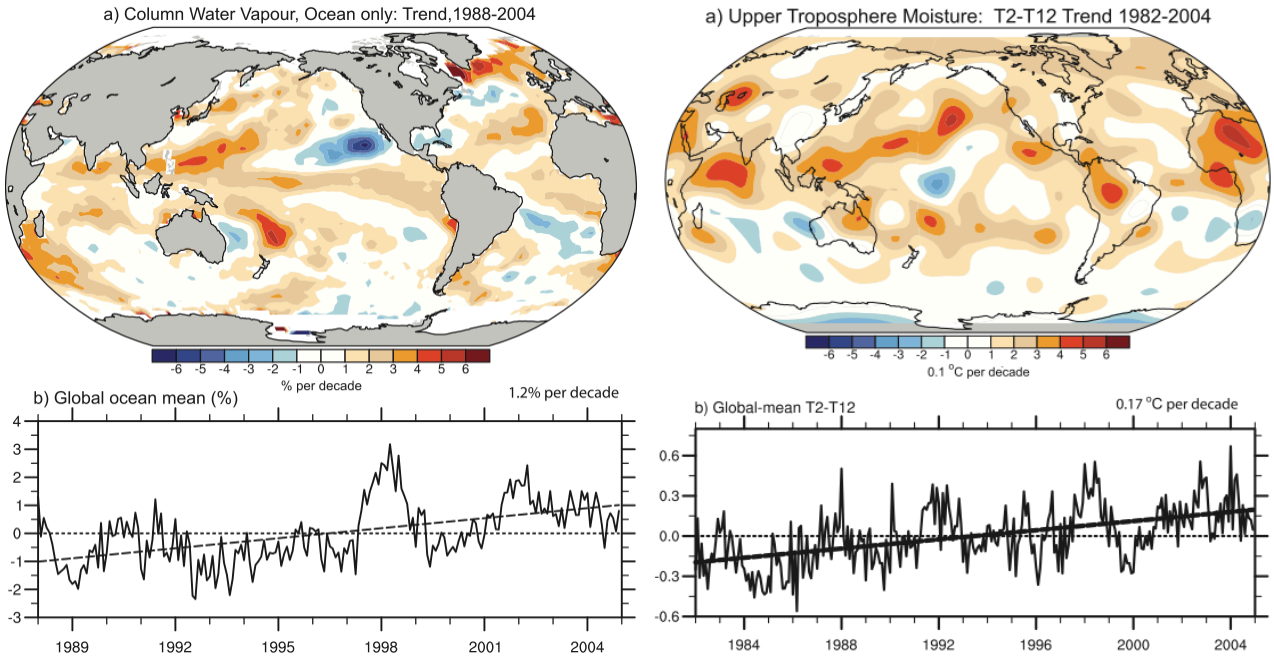

Figure 3: (left) Changes in columnar water vapor from 1988-2004. (right) Changes in Upper-Tropospheric moisture from 1982-2004. (Trenberth et al., 2007)

Engineering

High launch costs, extensive design and testing of spaceborne remote sensing systems result in costs on the order of $\$10^{5\text{-}6}$/kg (Scott, 2004). It is therefore of great importance to reduce the size and weight of space instruments in this field. Further, with the advent of micro and nano-satellite buses, high performance instruments compatible with these platforms will increase the utility of smaller budget spacecraft missions. SWSHS's are a type of FTS giving them high resolution and large throughput (Kramer, 2002). However, drawbacks of the FTS are a complex design involving mechanisms and moving parts in the optical system. SHS's don't have a mechanical scanning element, a monolithic glass prototype was developed to observe water vapour in the infrared (Lin,

2005). The SWSHS are etched into an IC making it a novel approach and an ideal candidate for space-based observations (Scott et al., 2009).

1.1.5 My Involvement

My involvement in the project has included both major and minor contributions to stages in the instrument's lifecycle. This included developing itemized requirements and goals for the project (listed below). I was involved in the development and requirements of the graphical user interface and the electronics functions. I created a conceptual design of a space version of instrument based off the requirements in order to estimate size, mass and energy of a smaller version of the instrument. I was responsible for the design of the telescope barrel, aspects of the optical bench and the graphical user interface. The assembly was my second largest contribution, which included the alignment of the detector and waveguide, the telescope barrel and waveguide as well as integrating all components into the chassis. My largest contribution was implementing calibration and retrieval algorithms. The bulk of my work was spent on the assembly and retrieval algorithms, with oversight provided by COM DEV along with contributions from the National Research Council. These aspects occurred throughout the development of the instrument. I also extensively tested the instrument in a laboratory setting. Several goals of the project that I was involved with included:

Goal 1: Development and building a prototype SWSHS chip and breadboard optical instrument at SHOW wavelengths

Goal 2: Investigate alternative method(s) for increased coupling efficiency

Goal 3: Build prototype spectrometer for SHOW waveband.

Goal 4: Build input optics for the SWSHS

Goal 5: Develop system packaging and build a prototype system

Goal 6: Develop inversion algorithms and calibration procedures for system using test data from laboratory tests of micro-SHOW linear prototype

Goal 7: Iterate design and build prototype high-throughput spectrometer for SHOW waveband.

Completion of these goals can be used as a measurement of success for the project. Quantitative requirements, where applicable, are outlined in the background of each of the design sections. The optics and electronic sections contain the most detailed quantitative requirements for the instrument.

1.2 Background

1.2.1 Satellite Observations of Water Vapor

A review of space based instruments capable of measuring atmospheric water vapor. The table below shows that there are currently 12 such instruments. When available, the viewing configuration, weight, size, power consumption, swath width, spectral bands and spectral resolution are included.

Table 1: Instruments that have made Water Vapor Measurements

Instrument	View	Weight	Size	Power	Swath	Spectral Bands	Spectral Resolution
HALOE	Solar Occultation (15~60-130km)	101kg	36in	N/A	N/A	2.5-11um	N/A
ACE-FTS	Solar Occultation	41kg	N/A	37W	1.25mrad (FOV)	2.2-13.3um	0.02cm^{-1}
MAESTRO	Solar Occultation (10-100km)	8kg	N/A	N/A	N/A	285-1030nm	1-2nm
MODIS	Nadir	228.7kg	1*1*1.6m	162.5W	2330*10 km	0.4-14.4um	N/A
GOMOS	limb	N/A	N/A	N/A	N/A	0.25-	N/A

						0.95nm	
MIPAS	limb	N/A	N/A	N/A	3*30km	4.15-14.6um	0.035lines/cm
TES	nadir and limb	385kg	1*1.3*1.4	334W	2.3*23limb	3.2-15.4um	0.00025cm^{-1}
SAGE III	solar occultaton	76kg	73*45*93cm	80W	N/A	0.29-1.03um	1-2nm
POAM III	solar occultaton	N/A	N/A	N/A	N/A	353.4-1018nm	N/A
MISR	nadir	148kg	N/A	117W	9 cameras	4 bands at 446, 558, 672, and 867	N/A
MAS	limb	N/A	N/A	N/A	N/A	N/A	N/A
SCIAMCHY	nadir/limb+ occultation	198kg	N/A	122W	limb 3*132km	(240 nm - 2380 nm	0.2-0.5

2. INSTRUMENT DESIGN

2.1 Introduction

The instruments primary functions are to (1) format light for input into the waveguide, (2) provide a spatially stable and robust interface between the waveguide and detector, (3) protect the waveguide and (4) provide a readout of the interferometer array (Robertson et. al., 2010b). The instruments subsystems satisfying these requirements can be categorized as:

a. the telescope assembly (**Figure 10**)
b. chassis (Figure 24)
c. optical bench (Figure 7)
d. electronics

Background information on each subsystem and details of my involvement in the telescope assembly, optical bench and electronics is described in the proceeding sections. Below is a block diagram of the structure of the spectrometer.

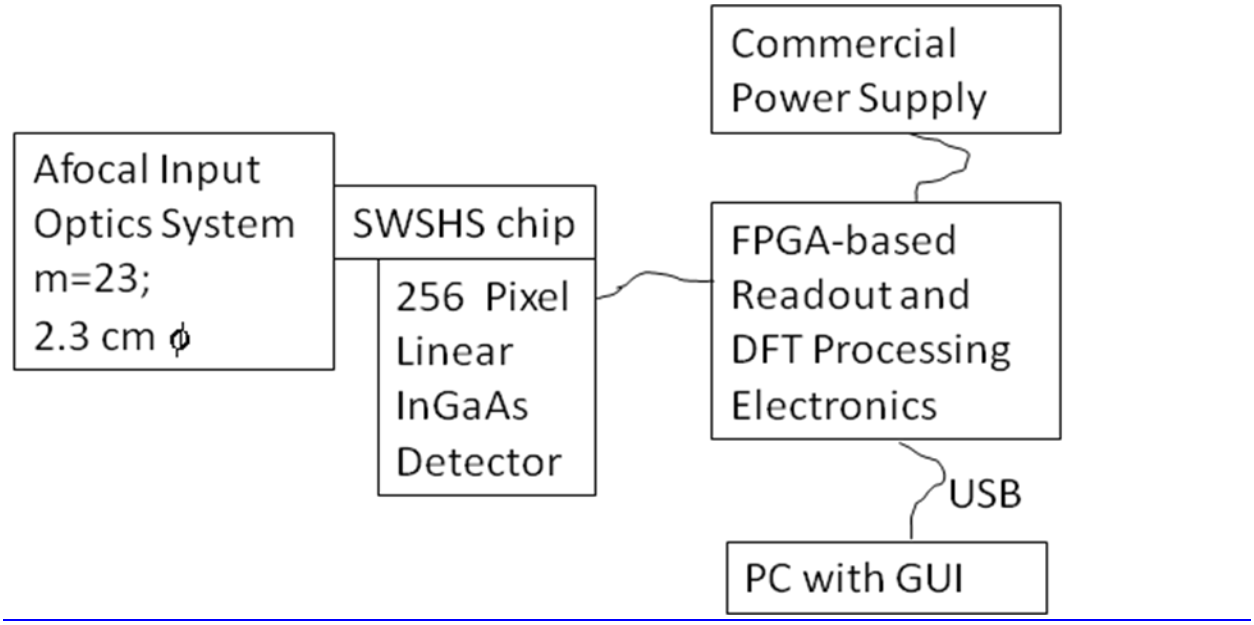

Figure 4: A block diagram of the structure of the instrument.

2.2 Optical bench

2.2.1 Introduction

This section describes the theory and design of the mechanical interface between slab waveguide and detector. It has undergone an iterative design process with three major productions over the course of several years. The optical bench comprises the optical processing core of the instrument. Components within the assembly include the slab waveguide, the optic bench, the detector and the

electronics. The optical bench serves as a structural element providing support for the slab waveguide-detector interface.

The optical bench in the instrument is the third generation of the component. Previous designs were used in a student led instrument prototype and as a part of the breadboard instrument created at the National Research Council. This section begins with an analysis of the previous generations of the optical bench, details the requirements of this version and a detailed description of the design concludes this section.

2.2.2 Background

The first model of the optical bench was used as a baseline design and for analysis for the second and third generations of the design. This design focusing on providing spatial support for the slab waveguide and maintaining a spatially stable connection between the detector and waveguide. As can be seen in Figure 5, the design resembles an L-bracket. This design was vibration and thermally tested as apart of a space qualification. An analysis of the design is given below.

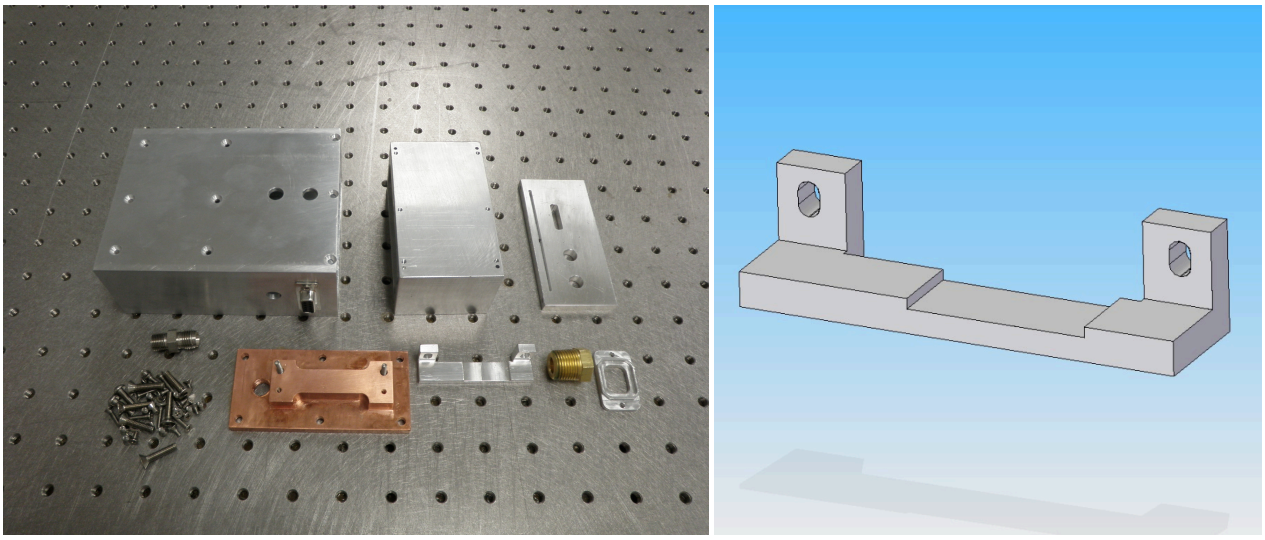

Figure 5: First generation (2009) instrument in parts (left) and optical bench design (right)

Benefits

a. Provided a robust spatial support

Drawbacks

a. The hardened and rigid epoxy connection between the optical bench and waveguide would likely induce stress in the waveguide when exposed to thermal fluctuations. This would shorten the lifespan of the instrument.

b. The design does not block stray light from entering detector. A makeshift baffle was introduced late in the assembly stage to correct for this.

c. Shifting was problematic during assembly with the optical bench, detector being mounted to the housing through the same screws.

The second generation of the design was used for the breadboard instrument at the National Research Council's Institute for Microstructural Sciences Laboratory in Ottawa, Ontario. It was designed to improve on the first generation. The second generation is shown in Figure 6 and is noticeably different than the first generation although provides similar functionality.

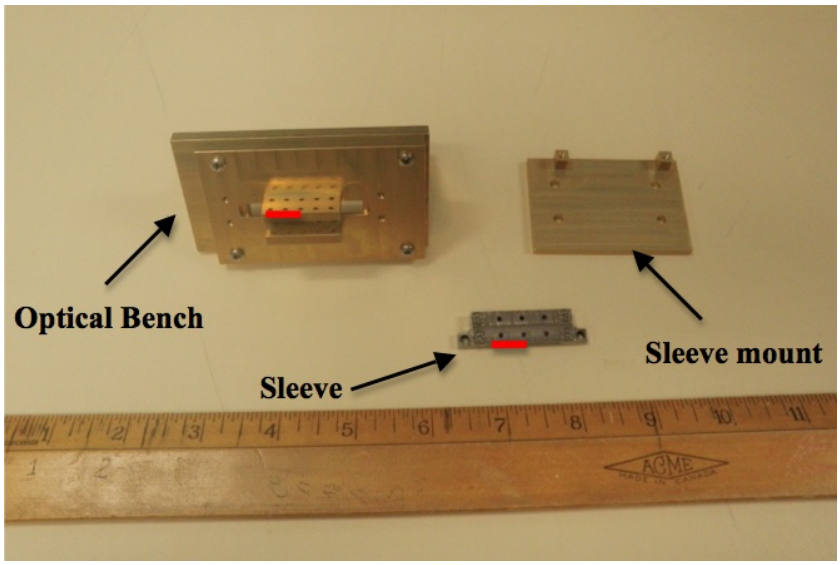

Figure 6: Second generation optical bench

This design was superior to the first generation. It provided the same robust support (although not space qualified).

Benefits

a. Provided a robust spatial support
b. Waveguide stability was secured by encasing it in a sleeve prior to alignment.
c. Stress experienced by the waveguide was eliminated by using Invar as the sleeve material and by using silicon gel as an interface between the sleeve and waveguide.

d. Shifting during assembly was eliminated by first connecting the detector to optical bench and later mounting the entire optical bench into the housing using separate brackets.

Drawbacks

a. Optical bench improved on blocking light, however many spaces existed that continued to allow light to enter.

2.2.3 Requirements

The third generation of the design had the operational requirements as follows (Robertson et. al., 2010b):

a. The bench shall provide a spatially stable waveguide-detector interface protecting against thermal and vibration stresses
b. The bench shall prevent stray light within the housing from reaching the detector.
c. The bench shall ensure that the mechanical support of the of the optical bench does not induce stress in the waveguide

2.2.4 Design

The design used in the instrument maintains alignment between the detector and waveguide. It was designed to use the beneficial aspects of the previous generations, and avoid the drawbacks. This design featured modified attributes from the previous generations including:

a. Waveguide sleeve
b. Using silicon for sleeve-waveguide bonding
c. Bonding towers
d. Epoxy for sleeve-tower interface which provides thermal insulation and a robust connection
e. Improved light baffling features
f. The interferometer arrays shape was changed to create a 90° elbow shape in hopes that stray light that enters the waveguide would exit the other side
g. Independent detector-optical bench and optical bench-chassis fastening mechanisms

The design is shown below in Figure 7.

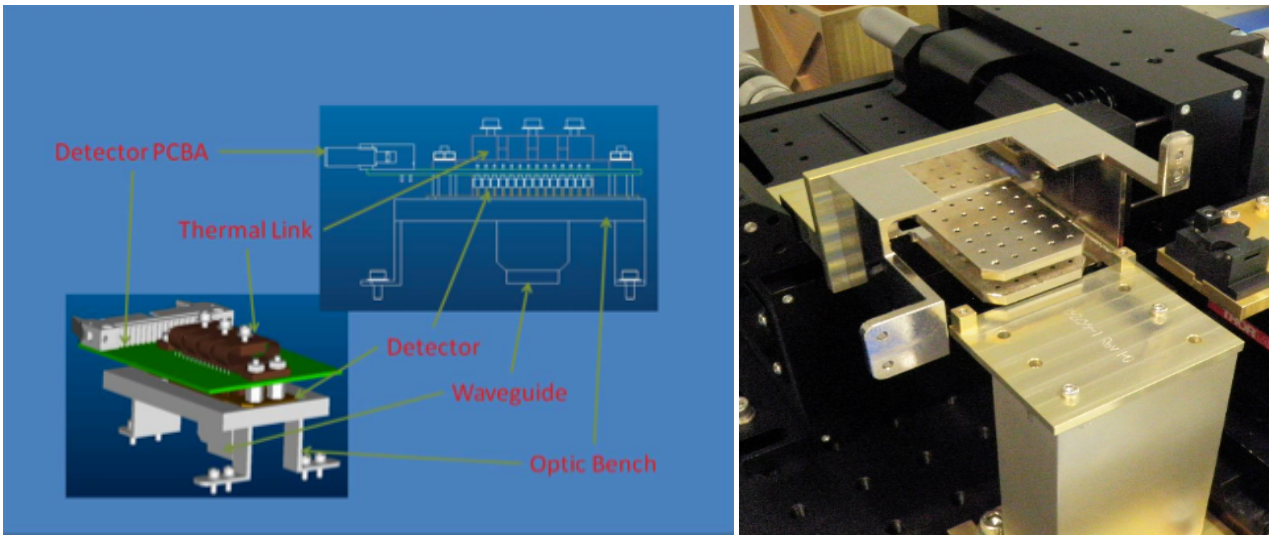

Figure 7: CAD of the third generation optical bench (left) during assembly (right)

(Robertson et. al., 2010b)

The optical bench also provided excellent support for the waveguide through the oversized bonding towers. The sleeve was also made to encapsulate nearly the entire waveguide only allowing it to protrude enough to allow for coupling to the detector array. The design of the optical bench also provides several degrees of freedom for alignment purposes. To minimize the effects of stress-induced birefringence within the slab waveguide, the optical bench was made from Invar, which will provide a high dimensional stability within the optical bench assembly. The silicon waveguide has a thermal expansion coefficient of 2.6ppm/$^{\circ}$C while Invar, depending on grade chosen, is capable of a similar coefficient. The material used to bond the waveguide to the optical bench offers flexibility by using silicone. This is a viscous material that will cure at room temperature and not change dimensions appreciably.

It should also be noted that the waveguide pocket was capable of being expanded to allow several waveguides to be stacked in order to further increase throughput or allow several spectrometers to exist within the instrument by using a 2D detector array. The benefits of stacked Slab Waveguide Spatial Heterodyne Spectrometers for space applications was foreseen by Scott et al. [Scott, A., 2004] in the context of planetary sensing.

A drawback of this design stemmed from the optical bench and waveguide being fabricated separately. From above, the optical bench was configured to hold a waveguide with an ‘L’ bend while the waveguide was opposite this. It was possible to rotate (or turnover) the waveguide 180° to correct for this however, the waveguide were no longer visible from above. In order to align the input optical fiber with the input of the waveguide, a small mirror was placed beneath the bonding

towers on the sleeve mount. This allowed the waveguide and fiber to be pre-aligned with all motions reversed.

2.3 Telescope Mount

2.3.1 Introduction

This section describes the theory and design of the structural element of the telescope. The purpose of the telescope was to format light for the input facet of the waveguide. I was involved in designing the casing for the 4 lens system. Also, the design of the optical system was significantly different than that of the first generation so an analysis of the first generation did not prove useful.

2.3.2 Background

The four-lens system telescope system was designed for solar occultation absorption sensing with an observational target wavelength of 1.3645 μm. The system designed is an Afocal Telescope Assembly, which formats light for input to the slab waveguide. The sun is half of a degree wide and the optical system has been designed with a larger field of view of ± 0.5 degree. The system was designed to block stray light from being detected, filter out-of-band radiation and provide uniform solar illumination in a single linear polarization to the waveguide input facet. The étendue of the optical system was designed to match that of the silicon on silica waveguides (Robertson and Scott, 2010d).

Since the optical system is not intended for imaging, but rather for waveguide coupling, the optical system was required to deliver a ray bundle in the image space that matches the numerical aperture (NA) of the waveguide. The linear array of waveguides measures 1.5 μm x 4 μm with apertures along a facet with centre-to-centre pitch of 8 μm. Therefore, the total length of the active area is ~960 μm. Each waveguide accepts and propagates a single, roughly Gaussian mode. The waveguides numerical aperture is 0.2. The following relationship needs to be fulfilled by the optical system:

$$NA_{wg} = n_{\circ} \times \sin(\theta) \qquad \textbf{Equation 1}$$

Where NA_{WG} is the waveguide's numerical aperture, n_o is the refractive index of the image space and Θ the chief ray angle of the edge field point at the waveguide. The maximum incident angle at the pupil is 11.5 degrees which gives a pupil NA of 0.2 which matches the waveguide NA.

The optical system consists of the telescope design with four spherical lenses. All four lenses are NBK10 from Schott glass having a relatively high index of refraction of 1.846 allowing the length of the assembly to be minimized. The high index of refraction also allows an anti-reflective coating of magnesium fluoride to be applied. The two objective and field lenses, L1 and L2, are contained within the barrel or the telescope. A cell contained within the barrel holds an additional two lenses, L3 and L4. The overall length of the assembly is 100 mm, from entrance pupil to the spectrometer input, and the maximum lens aperture diameter is 23 mm (Robertson and Scott, 2010d).

2.3.3 Requirements

The operational requirements of the telescope mount include:

a. The mount shall provide a spatially stable structure
b. The telescope assembly shall provide a stress free mounting system for the four-lens optical system design over a 40 degree temperature range.
c. The telescope design shall account for assembly and alignment of the four-lens system.
d. The telescope output will not interfere with the optical bench holding the slab waveguide. The chassis of the spectrometer will provide a surface to mount the telescope to.

Taken from Robertson and Scott (2010c).

2.3.4 Design

2.3.4.1 Thermal considerations

S30400 stainless steel was chosen for the telescope material instead of aluminum (same as the instruments housing) to better match the thermal expansion properties of the lens material. Therefore, for stainless steel to cycle 40 degrees and not induce a stress on the lens a thermal expansion calculation was completed:

$$dL = l_{\circ}\alpha\left(t_f - t_i\right) \qquad \textbf{Equation 2}$$

Where dL is the change in length, l_o is the initial diameter of the telescope barrel, α is the expansion coefficient, t_f is the final temperature and t_i is the initial temperature (Wikipedia, 2014). For the

largest section of the telescope barrel, using 27mm, 17.3 10^{-6} m/m K, 45°C and 25°C, a change in size of 9.342 μm can be expected.

A safety factor of 2 was used so that each lens would have 10 μm of spacing on either side. Note that for the smaller end of the telescope, this safety factor is closer to 4 because of the smaller diameter of the barrel at these points. This spacing is well within the optical tolerances of the system, which can be offset from center position by 100, 100, 75 and 86 μm for lenses L1 through L4 respectively.

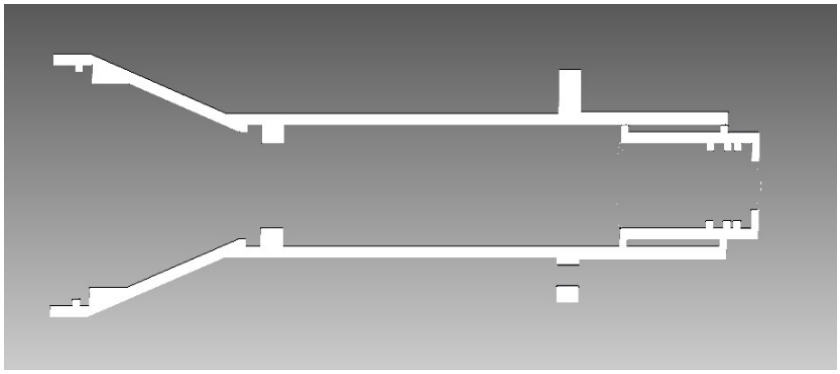

Figure 8: Cross section of the telescope mount.

2.3.4.2 Mechanical considerations

Each of the lenses were bonded to the telescope barrel using a silicone adhesive. Adhesive channels were designed into the telescope barrel to allow the silicone to be injected into the barrel in such a way that it would only bond the lenses around the edge. These can be seen in **Figure 8** as cavities recessed into the barrel structure.

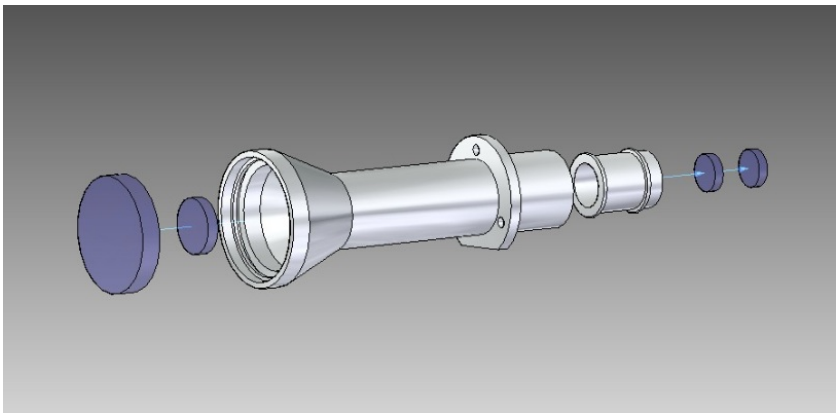

Figure 9: An exploded view of the telescope system including lenses

2.3.4.3 **Assembly considerations**

The design of the telescope barrel requires that first L2 (**Figure 9**) be first to be mounted then followed by L1.The insertable cell, which holds lenses L3 and L4 requires that L4 be inserted first followed by L3. The lens alignment procedure was not taken into consideration because the machining of the barrel allowed for accurate positioning of the lenses within the system.

Figure 10: Optical system detailing the 4 lens layout and mount (left) and fabricated barrel (right)

2.4 Graphical User Interface

2.4.1 Introduction

A graphical user interface (GUI) for the user of the host computer allowing control of the instrument and data was created. This section describes the user interface details between the host PC and electronics onboard the SWISH spectrometer. The user interface is required to act as a front-end graphical representation of commands and telemetry that permits intuitive use and control of the SWISH spectrometer. The GUI was designed to have a straightforward layout capable of presenting all data from the spectrometer in a meaningful manner. It simplifies usage of the spectrometer by sending multiple commands to the spectrometer though a single click when appropriate (Sinclair et. al., 2009).

2.4.2 Requirements

The following details the requirements of the GUI (Robertson and Scott, 2010b):

a. The host PC GUI shall implement a control interface with the SWISH spectrometer as per the External Interface Control Document for COM DEV Ltd. project 50142 (Appendix 9.6). The host computer interface with the SWISH spectrometer interface is used for controlling and monitoring the internal electronics of the SWISH spectrometer.
b. The host PC GUI shall provide real-time acquisition of data and environment variables. This should include indications of saturation vs. low signals as well sensing temperature data. The GUI shall be capable of controlling parameters of the spectrometer including the integration time, sample rates, the detector temperature and frame averaging.
c. The host PC GUI shall maintain communication protocols resilient to errors through the use of a data sequence counting variable, checksum and other data validation techniques.
d. The GUI shall allow the user to specify a uniquely-named data file to store either raw telemetry data or processed data. This file shall include headers indicating the time of data acquisition, temperature of the detector and waveguide for each frame as well as an average of each during acquisition. This will also include the integration setting of the spectrometer, frame averaging number and signal strength during each data frame.
e. The host PC GUI shall enable calibration and data processing procedures. The host PC GUI shall allow calibration coefficients to be derived and seamlessly integrated into processing software in real time.

2.4.3 Design

2.4.3.1 Main Control Panel

The main control panel's primary function is to upload parameters to the spectrometer and switch the spectrometer into operational mode. The is the main control of the spectrometer with functions that include starting and stopping data acquisition, setting the refresh rate, integration time and frame averaging parameters. All of these upload parameters to the instrument except *refresh rate*, which is used by the GUI itself.

The control panel accomplishes this through a series of background commands. To begin acquiring data, only the "capture" button needs to be clicked. When this happens, three commands are sent the instrument; two upload the sampling and frame averaging parameters and the third switched the instrument into operational mode. For ease of use, a default sampling rate and integration period is automatically displayed. An image detailing the panel is shown in Figure 11.

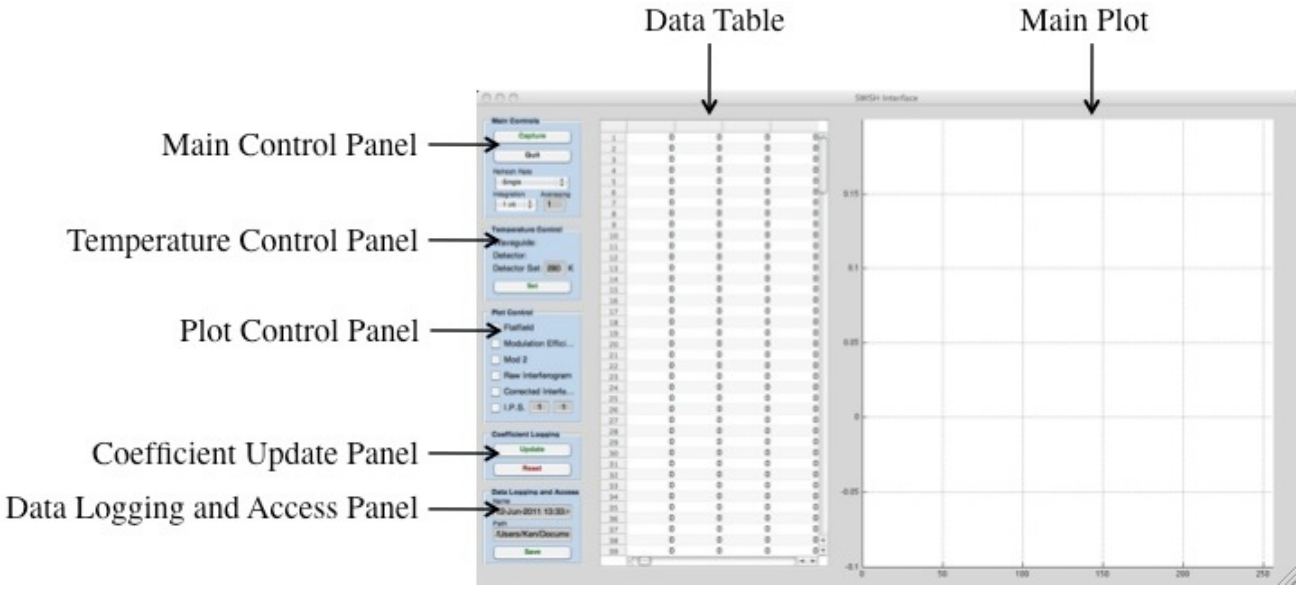

Figure 11: Overview of data handling and access through the user interface.

2.4.3.2 Temperature

The temperature control panel has the dual purpose of displaying the waveguide and detector temperatures as well as setting the detector temperature. This must be set before the instrument is switched into *Operational Mode* since it is not possible to write coefficients to the instrument while in this mode. An image detailing the panel is shown in Figure 11.

2.4.3.3 Plot Control

The Plot Control panel controls the flow of data from the instrument to the GUI. It allows the user to plot any raw or processed data from the Data Table. Through each refresh cycle, this menu is checked and any selected variables are read from the data table file and plotted. This panel was primarily useful during calibration of the instrument when it was desirable for several variables to be

plotted at once while in operational mode, only the retrieved spectrum may be wanted. Each time new data is obtained and processed, the plot refreshes only plotting selected data variables to the main plot. An image detailing the panel is shown in Figure 11.

2.4.3.4 Data Logging and Access

The Data Logging and Access panel is used to specify a file to save processed data to or read from an archived data from a file. Each saved file contains a header that indicates the time and the settings the spectrometer was operating under during the time of acquisition. Each processed data frame contains the temperature of the waveguide, temperature of the detector and average power obtained through the monitoring waveguides. An image detailing the panel is shown in Figure 11.

2.4.3.5 Data Table

The Data Table contains all coefficients, raw and processed data and is updated at the Refresh Rate specified in the Main Control panel. All of this data can be plotted using the Plot Control panel and also can be updated by simply entering new values. To do this, the automatic updating needs to first be stopped by either pressing the ‘stop’ button or changing the refresh rate to ‘single frame’ and pressing ‘capture’. The columnar data within the table includes coefficients to correct the received data for interpixel spillage, dark current as well as the raw and corrected interferograms. An image detailing the panel is shown in Figure 11 above.

2.4.3.6 Plotting

The main plot displays all pixel information received from the spectrometer as well as any correction coefficient data from the table. The main plot refreshes itself as new data is obtained from the buffer. An image detailing the panel is shown in Figure 11 above.

2.5 Conclusion

The hardware design of the instrument was effective in achieving the broad overall goals. The design also accounted for the complicated assembly procedure required for such a device. For instance, the alignment of the lenses in the telescope system, was considered. Improvements could be made to the overall size and more so the weight of the instrument, both the optical bench and telescope mount could have their mass reduced without sacrificing performance. The communication of the instrument did implement all required functions, however did not implement all aspects initially discussed, such as onboard processing of data.

3. ASSEMBLY

3.1 Introduction

The instrument had many components, a few of which needed to be assembled in a particular order and within several microns accuracy. Being a prototype instrument, many procedures were created and many hurdles needed to be overcome along the way. I was involved in several major aspects during the assembling of the SWISH Spectrometer including the optical bench alignment, telescope alignment along with several other smaller contributions. This involved using experience I had

previously gained, COM DEV personnel and resources. A description of the assembly processes is described in the proceeding section.

3.2 Optical bench alignment

3.2.1 Introduction

The optical bench assembly is comprised of the detector array, the slab waveguide and the optical bench itself. It is the most sensitive component to assemble. Over the course of my involvement in this project and previous slab waveguide projects, I designed and executed three alignments in three different laboratories, each time with different equipment and software. Each involved using micropositioners to align a slab waveguide with a detector to within at least 5 μm accuracy.

3.2.2 Background

The interferometers and monitoring waveguides have an output pitch matching that of the linear detector array. This allows individual waveguides to align with corresponding pixels. The output of each interferometer, Figure 12a, is significantly smaller than the size of individual pixels, Figure 12b. The waveguide array was fabricated using 4 μm wide and 2.2 μm high silicon-on-insulator (SOI) ridge waveguides. Each interferometer output measures 4 μm in width and 2.2 μm in height compared with the pixels 25 μm width and 500 μm height. Notice in Figure 12b that only 50% of the surface area is active pixels.

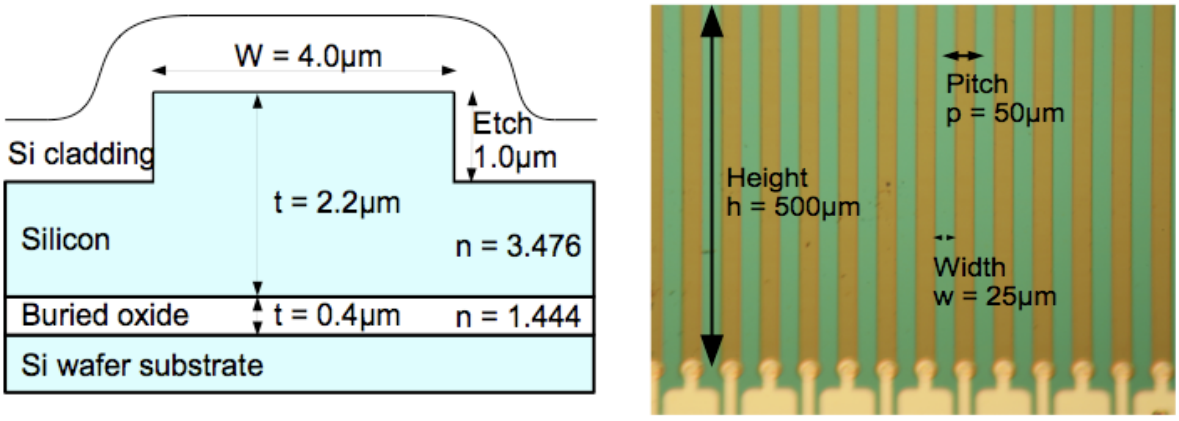

Figure 12: Dimensions of a single waveguide output (a) and the detector pixel layout (b). Detector photo is courtesy and copyright 2010 by Sensors Unlimited, Inc.

The optimal distance between the waveguide and detector pixels is a factor of the far field distribution of the signal. The far field distribution can be calculated from the refractive indices of the waveguide using Snell's Law.

$$\frac{\sin\theta_1}{\sin\theta_2} = \frac{n_1}{n_2} \qquad \textbf{Equation 3}$$

Where Θ_1 and n_1 are within the waveguide and Θ_2 and n_2 are in the space between the waveguide and detector. This is illustrated in **Figure 13** below. The index of refraction of the waveguide is taken to be 3.5 and the free space as 1.0 if it is air.

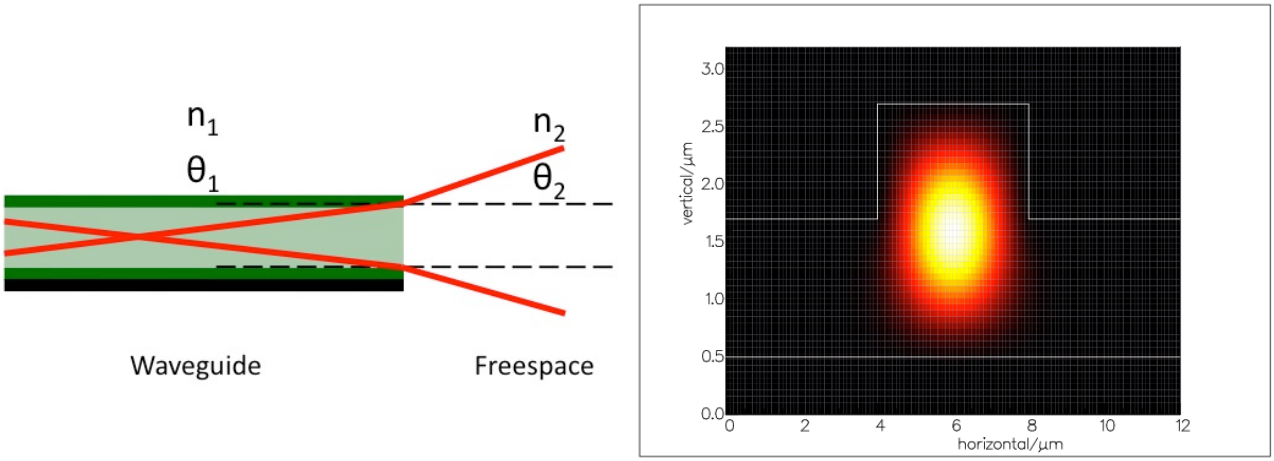

Figure 13: Far field distribution of the waveguide

The horizontal Full Width at Half Maximum (FWHM) of the propagation signal can be found from either contour plots of the far field distribution or a calculation using the refractive index. The FWHM of the signal for distances of 50 µm, 100 µm, 123 µm 200 µm and 400 µm was found to be 20.3 µm, 40.7 µm, 50 µm, 81.4 µm, 162.8 µm respectively. If the source of the signal were located between two pixels in dead space, the field distribution would have needed to be between 40 µm and 100 µm wide. As the waveguide-detector separation decreases, the beam width at the detector surface is reduced and increases as the separation is increased. From this, the optimal waveguide-detector separation can be calculated. The optimal beam width at the detector matches the pixel width of 50 µm, which occurs at a separation distance of 123 µm. These distances are shown in Table 2.

Table 2: Far field distribution of the waveguide

Distance (μm)	Beam width at detector (μm)
50	20.3
100	40.7
123	50
200	81.4
400	162.8

Atypical situations can arise from the distance being too great, too small or off center. Four of these are shown in **Figure 14**. As can be seen in **Figure 14** (A), when the waveguide-detector separation is less than 50 μm, it is possible that that signal may reflect off dead areas between the pixels and again off the waveguide with the signal then illuminating pixels adjacent to the objective. In this situation, the signal increases to a certain point, then the signal can be observed to be entering adjacent pixels. This means that the waveguide-detector is very small and there is risk of the waveguide contacting the detector. As can be seen in **Figure 14** (B), when the waveguide-detector alignment is off, translating the waveguide closer or farther will produce weak changes in the signal, however the signal can be further maximized through lateral translations. **Figure 14** (C) depicts the ideal situation where the waveguide-detector separation is 123 μm and on center. **Figure 14** (D) depicts the most common situation that occurs during alignment where the waveguide is too far from the detector and the signal illuminates adjacent pixels or dead space between pixels.

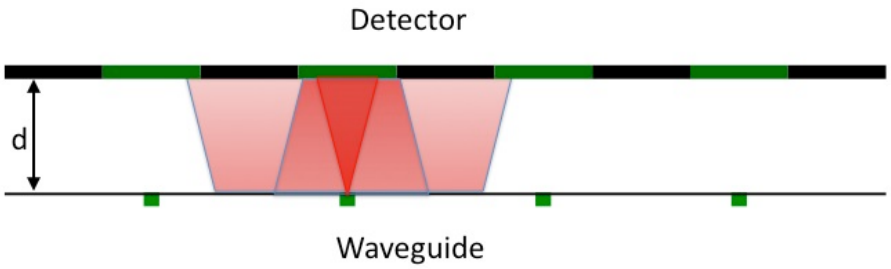
Detector
d
Waveguide

A

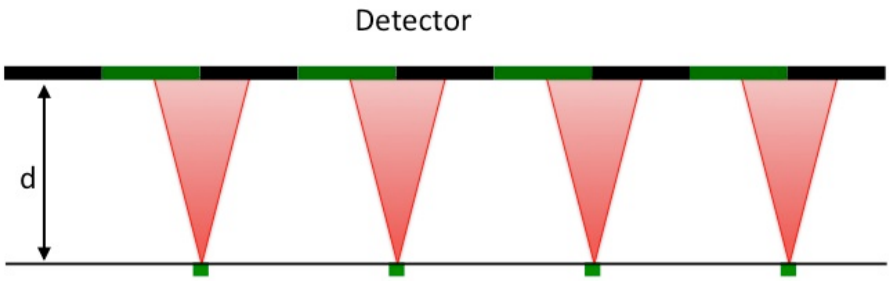
Detector
d
Waveguide

B

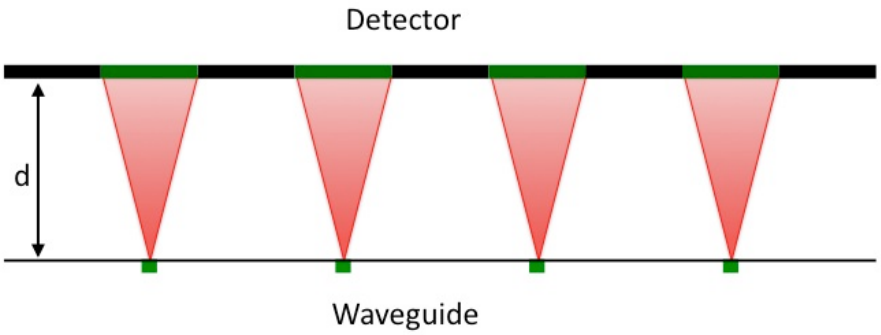
Detector
d
Waveguide

C

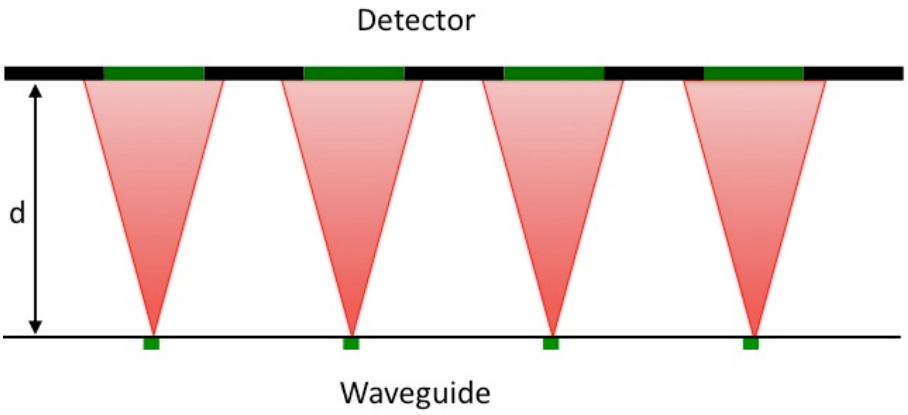

D

Figure 14: Waveguide signal distribution as a function of distance. (A) <50 µm separation (B) off center alignment (C) ideal 123 µm separation and (D) >123 µm separation

3.2.3 Results

3.2.4 National Research Council Preliminary Alignment

A breadboard spectrometer was constructed at the National Research Councils Institute for Microstructural Sciences (NRC-IMS). It was intended to ascertain alignment procedures and demonstrate preliminary results of a monochromatic input signal. A slab waveguide array of 50 Mach-Zehnder interferometers, each with a single output provided a discrete Fourier Interferogram of incoming light into 50 contiguous pixels of a Sensors Unlimited SU256LSB-1.7T1 InGaAs linear detector. The slab waveguide was designed for the 1550 nm wavelength range and had a theoretical wavelength resolution of 0.43 nm and spectral range of 10.86 nm.

For testing purposes, the waveguide contained 11 “pass-through” waveguides with no interferometers. These were evenly distributed through the interferometer array to allow the

distribution of light across the input aperture to be monitored and aid in the alignment procedure. Drive electronics and software controlled the temperature, exposure time and provided readout of the full detector array. A live shot was displayed and then stored in a time-tagged file. The setup is shown in **Figure 15** below. The drive electronics for the detector system in this test were the Argus 1000 Electronics provided by Thoth Technology.

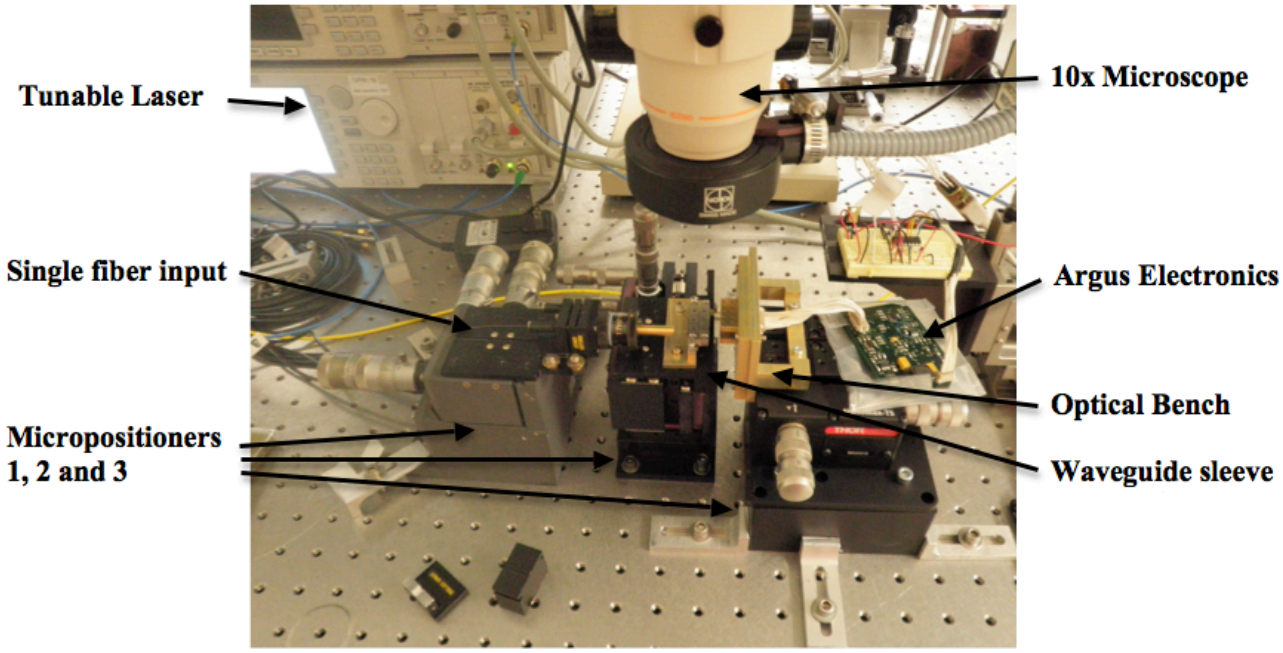

Figure 15: Alignment setup at the National Research Councils Institute for Microstructural Sciences

The waveguide needed to be bonded to the sleeve and is documented in Appendix 9.1. The mid-procedure alignment is shown in **Figure 16** (left) with the waveguide sleeve still attached to the mount and the final aligned optical bench **Figure 16** (right).

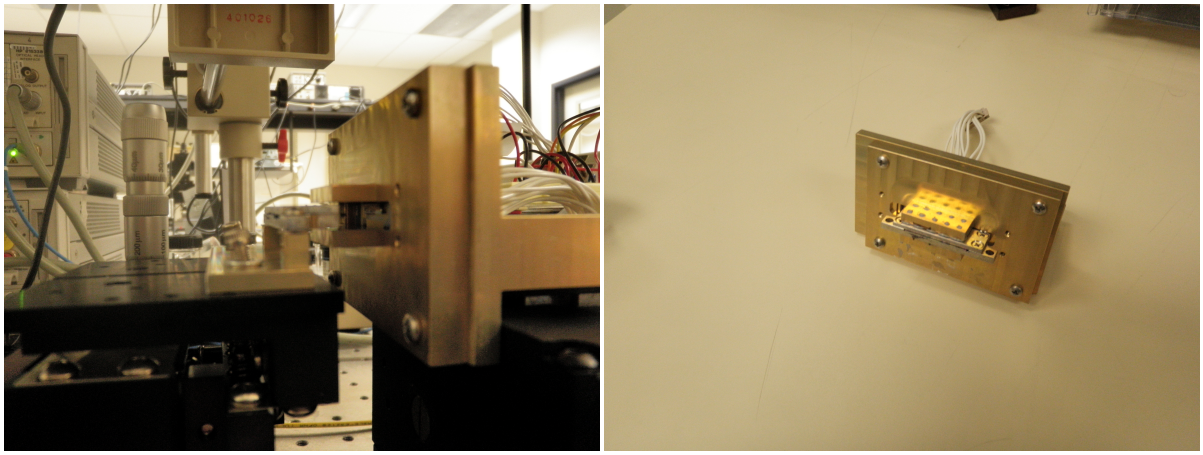

Figure 16: Alignment setup at the National Research Councils Institute for Microstructural Sciences

The procedure of attaching the waveguide to the mount involved using three tri-axis micropositioners, each with 0.1μm accuracy, to first align a single fiber input with a single interferometer on the slab waveguide and then aligning the detector relative to the waveguide. The pass-through channels within the waveguide typically provide the strongest signal of all the waveguides within the array. Pass-through waveguides 1 and 11 are also the first and last waveguides within the array. For these reasons, these waveguides were used to align the slab waveguide with the detector. A single fiber was used to illuminate the input of the first monitoring waveguide and was accurately coupled with the waveguide by repositioning it and maximizing the signal received at the detector. The detector was then repositioned in a similar fashion, which allowed the output from the monitoring waveguide to illuminate a single pixel. The results of illuminating the end monitoring waveguides 1 and 11 can be seen in Figure 17. Note the 61 pixel difference between the waveguides indicating the position of the waveguide within the detector array.

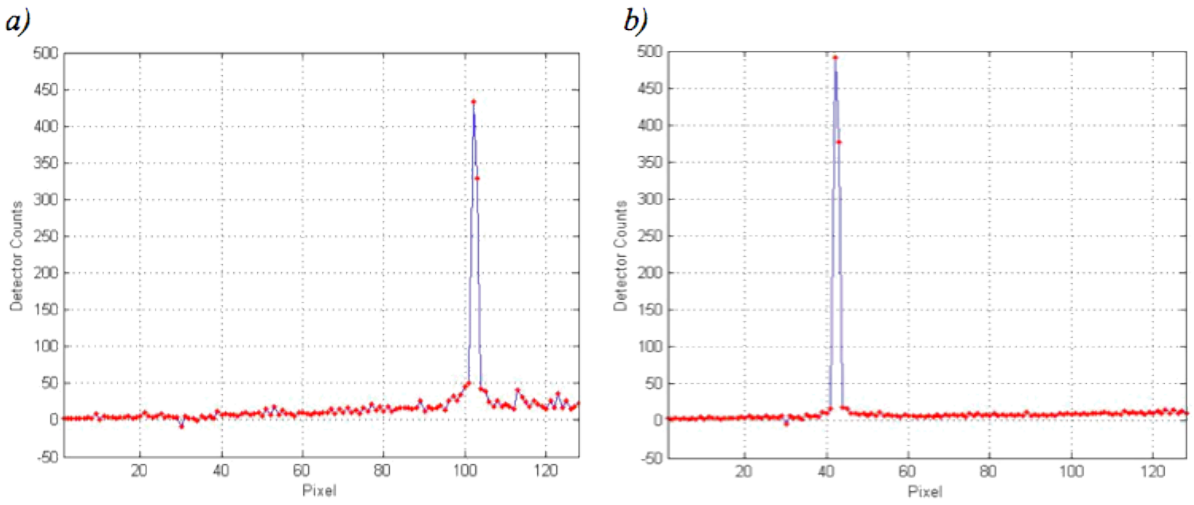

Figure 17: Alignment results from illuminating monitoring waveguide 1 (a) and monitoring waveguide 11 (b).

The data collected and displayed in Figure 17 also accounts for an initial measurement of the photo-response non-uniformity and dark signal master frame subtraction. The master frame consisted of an average of 1000 frames.

Although the maximum detector count varies by nearly 13%, the signal ratio of each of the two neighboring pixels in each case can be found to nearly equal at 0.765. This ratio of signal between neighboring pixels is ideally 0 and any value above this indicates that the waveguide is not centered directly in front of a pixel and that the output of the waveguide is located a distance from the detector. It has been found that to achieve a ratio of less than 0.01, assuming the waveguide is located directly on the center of a pixel, the waveguide will have to be less than 150 μm from the

detector array. If the waveguide is located beyond 200 μm from the array, 10% of the signal will be received on each of the neighboring pixels. Because 90% of the total signal was received on only two pixels, the high signal ratio can be attributed to a waveguide offset along the linear array rather than being located a distance from the detector array. If it were assumed that the output of the waveguide was located above dead space in the detector, a high signal ratio between two pixels can be obtained when the waveguide is 150 μm from the detector array. This would explain the high signal ratio while only illuminating two pixels.

From far field calculation, it can be found that the detector was located between 150 μm and 400 μm above the detector. From the data presented in Figure 17, if five adjacent pixels centered on each of the maximums are integrated, the total signal strength is 902 counts for monitoring waveguide 1 and 914 counts for monitoring waveguide 11. This indicates nearly equal signal strength was received at the detector in each case however the signal was distributed over one or more pixels on the array. This implies that monitoring waveguide 1 was located a further distance from the detector array than monitoring waveguide 11.

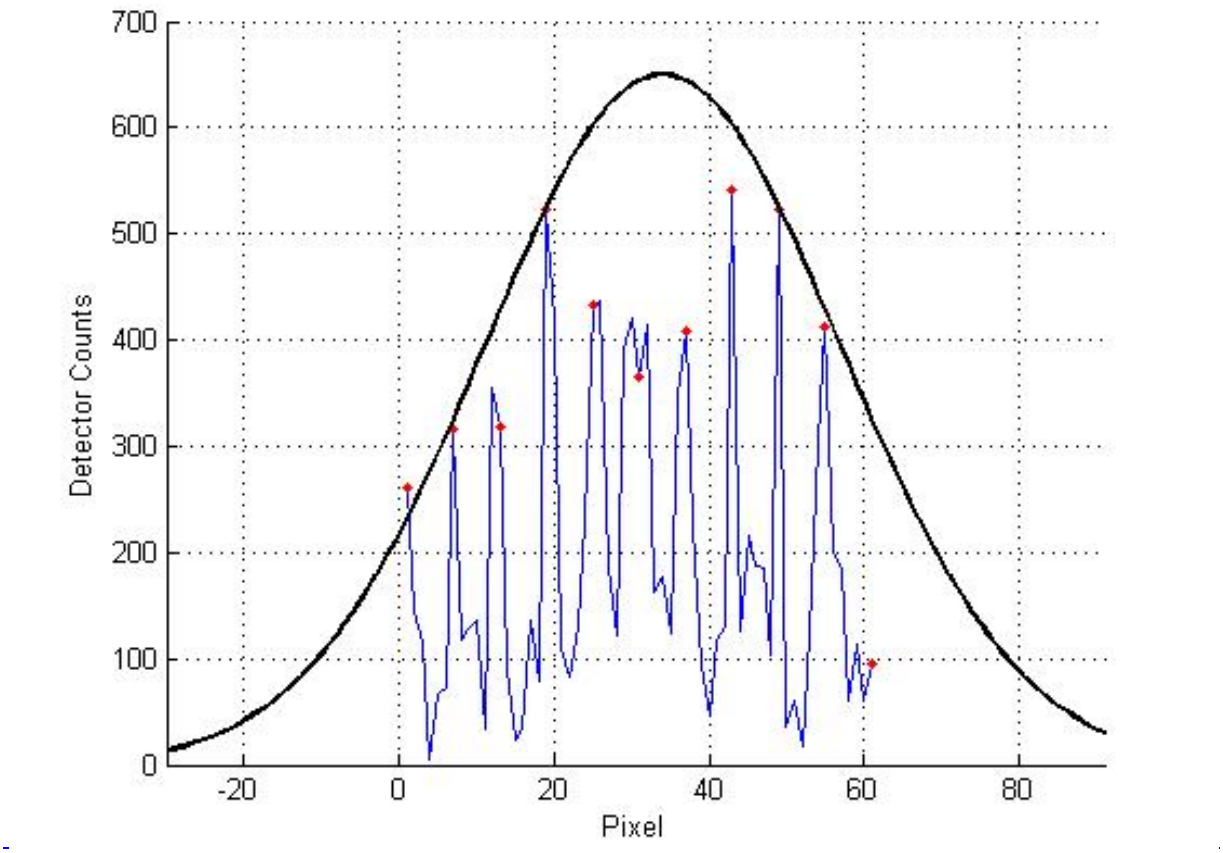

Figure 18: Results of a monochromatic input signal (blue). A Gaussian curve (black) overlaying the data and monitoring waveguides (red points).

A monochromatic signal from a tunable laser was fed into a lensed fiber and illuminated the input facet of the waveguide. This provided a crude method of coupling light to all of the waveguides simultaneously. Due to the beam propagation within the fiber, the mode intensity distribution is Gaussian shaped. This can be confirmed through observation of the 11-waveguide monitoring channels shown in red in Figure 18. A Gaussian curve shown in black in Figure 18 illustrates the nature of the mode distribution intensity of the input signal. The remainder of the pixels represents

the power interferogram of 50 MZIs. The layout of the MZI output ports is not sequential along the detector.

During alignment, the tuneable laser was scanned over a small passband and the output power from a monitoring waveguide was recorded. The results of this are shown in Figure 19. A oscillation in the signal can be observed. This phenomena is known as Fresnel reflections and are the result of internal reflections occurring at the input and output facets of a waveguide and causing interference.

$$R = \left(\frac{n_1 - n_2}{n_1 + n_2} \right)^2 \qquad \textbf{Equation 4}$$

Where n_1 and n_2 are the indices of refraction for the two medium, R is the percent of internally reflected signal. In order to reduce internal scattering and narrow the far field signal, the possibility of using an index matching gel was investigated. By increasing the refractive index of the free space between the waveguide and detector by using an index matching gel, which would decrease the amount of internally reflected signal and also decrease the signal divergence allowing the waveguide-detector distance to be larger. The effect of using the index matching gel on the output signal is shown in Table 3.

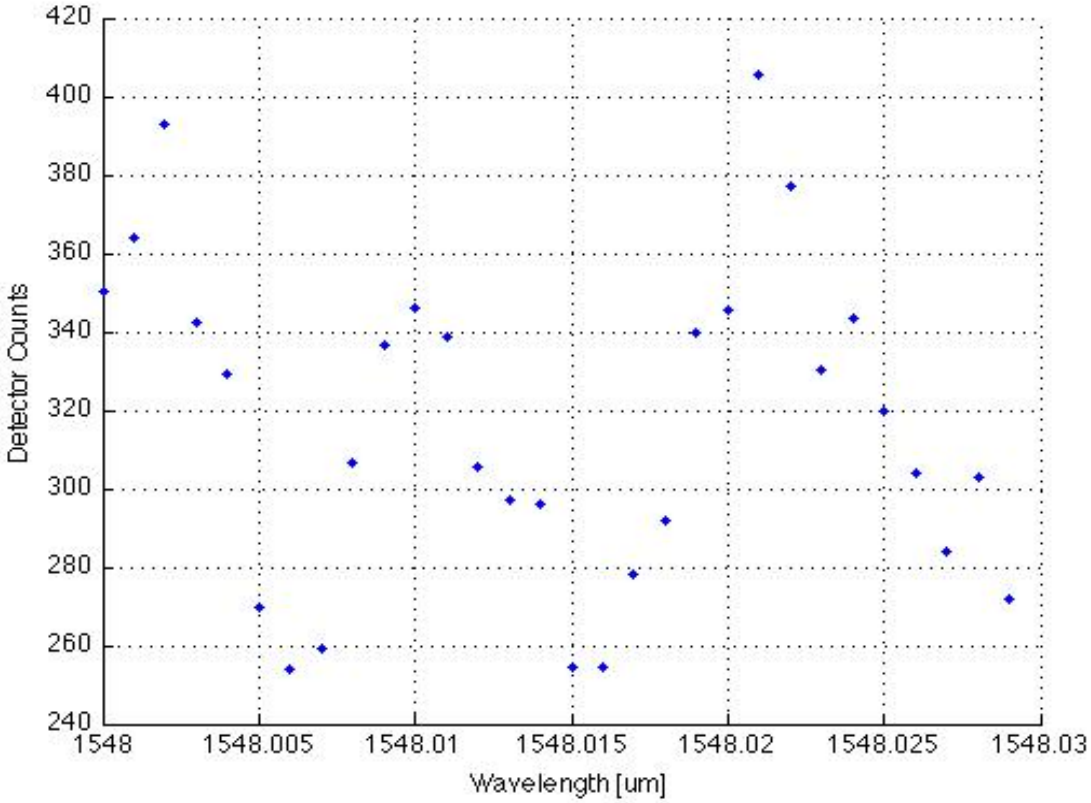

Figure 19: Internal interferometer reflections resulting in output interference.

The waveguides index of refraction is 3.5, the gel has an index of refraction of 1.7 and air is 1. From this, it can be calculated that 31% of the signal is reflected when the medium is air and it is reduced to 12% when the index matching gel is used. Reducing the reflected signal by 18% is a significant improvement. From Figure 19, the maximum signal is about 400 detector counts and the minimum is about 260 counts indicating that this causes over a 30% variance in signal from these reflections.

Table 3: Far field distribution of the waveguide using index matching gel

Distance (μm)	Beam width at detector (μm)
50	11.8
100	23.6
123	29.0
200	47.2
400	94.5

The index matching gel was Thixotropic Optical Gel OC-462. This gel was chosen due to wide operating temperature, low absorption in the passband, its chemical stability, it is non-conductive and has a high an index of refraction. It was found that the gel was difficult to apply properly resulting in bubbles existing in the medium. This presumably resulted in a large degradation in the signal. It was concluded that using this gel had risks that outweighed the benefits and it was decided to not use this gel in the final assembly of the instrument.

3.2.5 COM DEV Final Attempt

The alignment of the optical bench for the field instrument took place at COM DEV's facility in Ottawa. Similarly to the NRC, the procedure of attaching the waveguide to the mount involved using three tri-axis micropositioners, each with 0.1 μm accuracy. The setup also included a free space

monochromatic laser that was coupled to the fiber optic cable at the rear fiber mount. The setup also takes into account the waveguides 90° bend. This can be seen as the elbow shape between micropositoners 1 and 2 relative to micropositioner 3 and the optical bench. The entire setup is shown in **Figure 20** below.

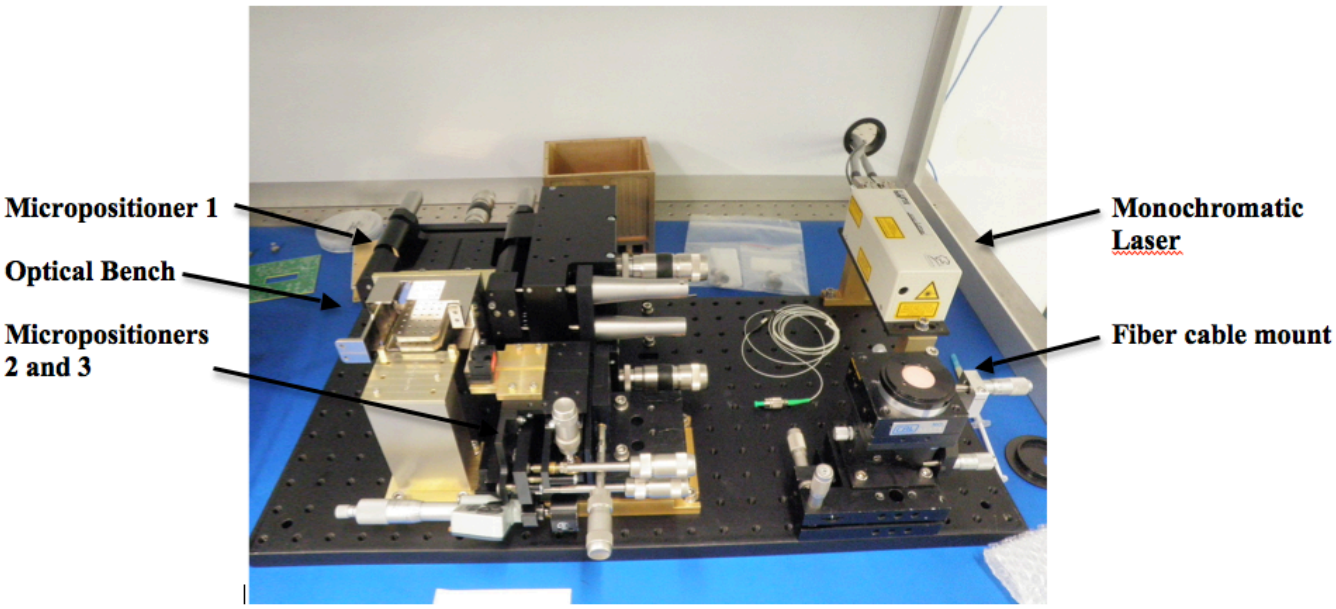

Figure 20: Alignment setup at COM DEV Ltd.

After the laser was coupled to the fiber, the fiber was aligned with a monitoring waveguide. Unlike at the NRC, there was no microscope capable of resolving individual waveguides so the alignment was accomplished using a NIR camera and a lens to focus the output from the waveguide.

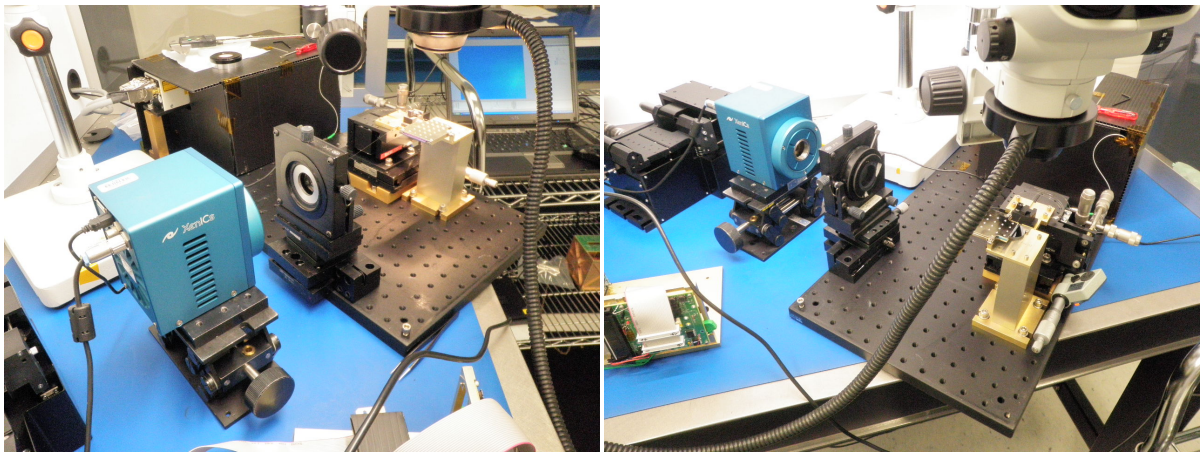

Figure 21: Fiber alignment at COM DEV Ltd.

Without being able to discern individual waveguides, tracking the fiber along the input facet while monitoring the camera's output allowed the fiber to be moved from one end of the waveguide to the other. The difficulty was also increased with the newer version of the optical bench since it was enclosed and did not allow for any visual pre-alignment. An illustration depicting this is shown in **Figure 22**.

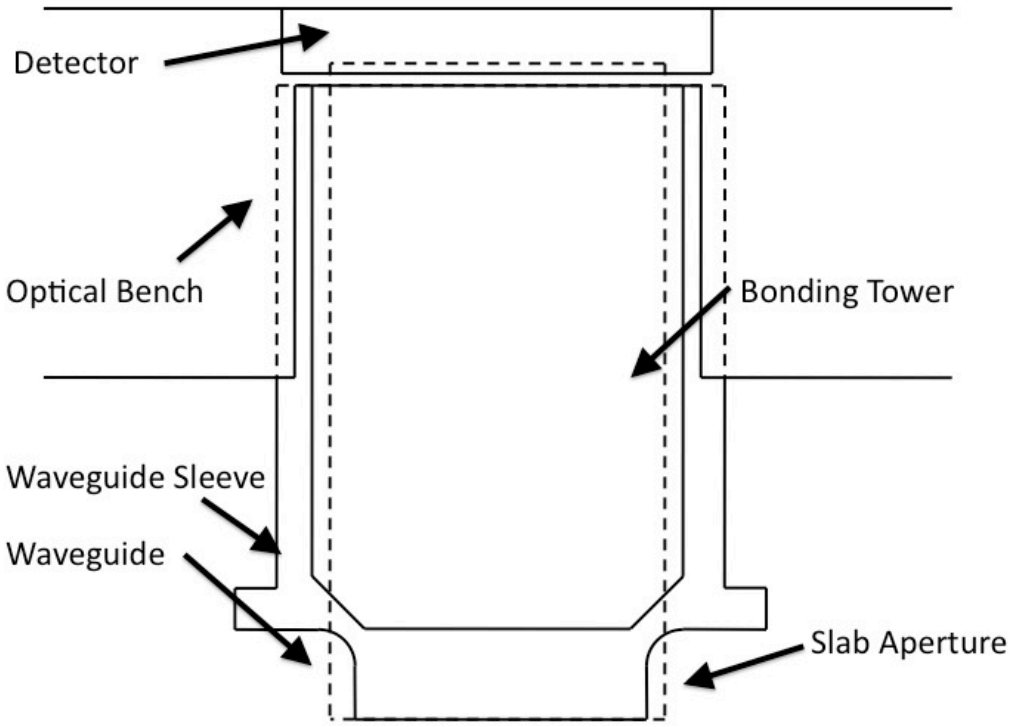

Figure 22: Illustration of the hardware viewed from above during alignment

The alignment results of illuminating monitoring waveguide 1 and 11 are shown in Figure 23. The data collected accounts for dark signal master frame subtraction. The master frame consisted of an average of roughly 1000 frames. For monitoring waveguide 1, adjacent waveguides receive 11% and 66% of the signal. This high ratio, is suspected of being the result of a fracture in the waveguides output facet and it was not possible to minimize this further. Monitoring waveguide 11 had noticeably better results with adjacent waveguides receiving only 0.58% and 1.15% of the waveguides output.

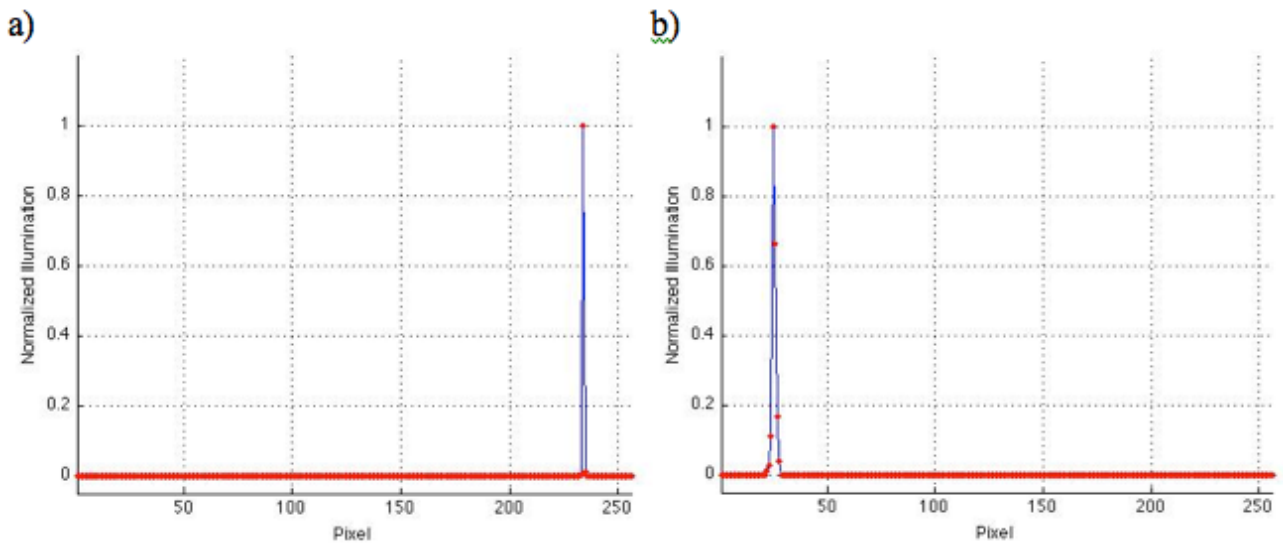

Figure 23: Alignment results from illuminating monitoring waveguide 1 (a) and monitoring waveguide 11 (b).

3.3 Telescope Alignment

3.3.1 Introduction

The telescope assembly setup, shown in Figure 24, shows the monochromatic laser illuminating a collimator. This provides the input beam to the telescope that is mounted on a tri-axis positioner. The SWISH spectrometer is mounted behind the telescope while the alignment can be finalized.

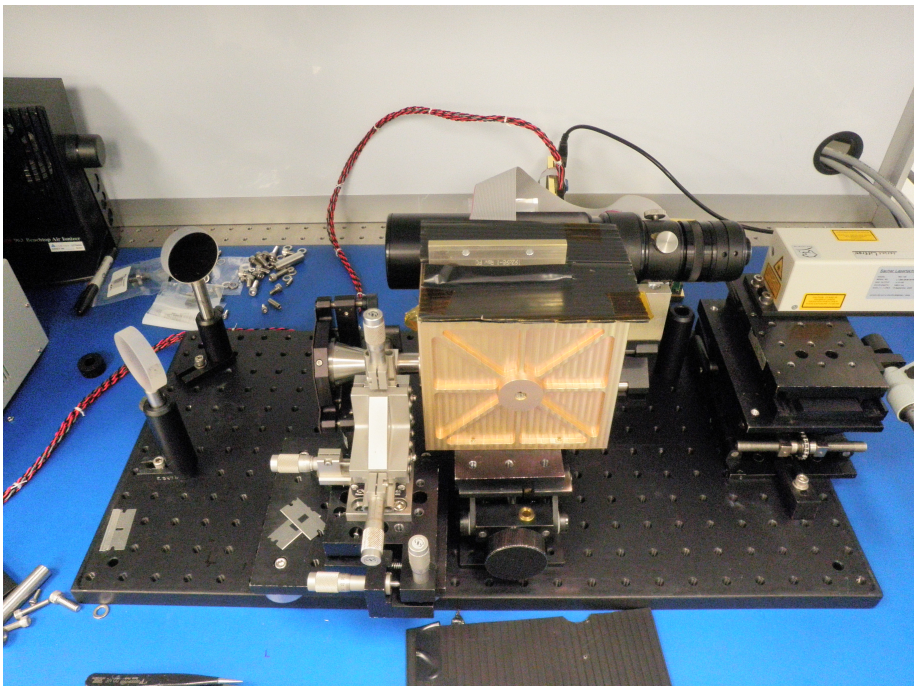

Figure 24: Telescope alignment setup.

A NIR camera was first used to align the input beam with the collimator and mask. To accomplish this, the NIR camera was placed in front of the telescope as shown in Figure 25 below.

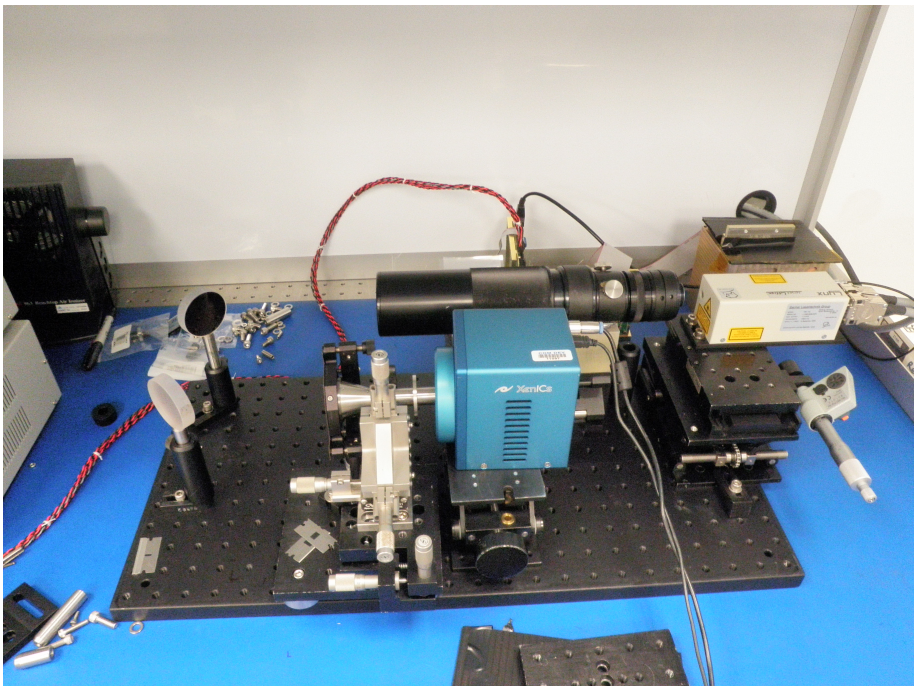

Figure 25: Telescope alignment setup.

During this procedure, it was discovered that light was entering and propagating through the waveguide. Due to the uniformity of the stray light observed along the detector, it was expected that there was a good deal of internal reflection occurring. This was caused by an unforeseen issue regarding the blocking of stray light was that the waveguide was transparent at the 1.36 region. A mask was constructed with the purpose of attempting to block stray light from entering as much of the slab as possible. The mask was created using magnets and razor blades, which allowed the razor blades to be adjusted to block the maximum amount of stray light. It was possible to block the area around the input facet to within 10 microns however, light could enter the slab from between the waveguides. This light would propagate through the waveguide and some would exit into the detector. The mask is shown in Figure 26.

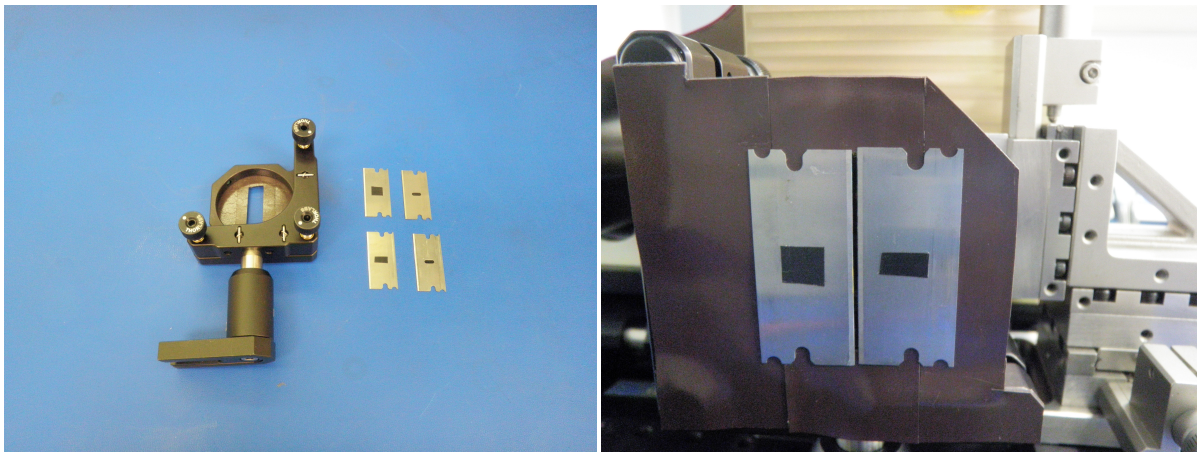

Figure 26: Mask design.

The collimated beam is shown in **Figure 27** (left) and with the mask in place **Figure 27** (right). It was possible to block nearly all of the light entering around the periphery of the waveguides, however it was not possible to block light entering between the waveguides.

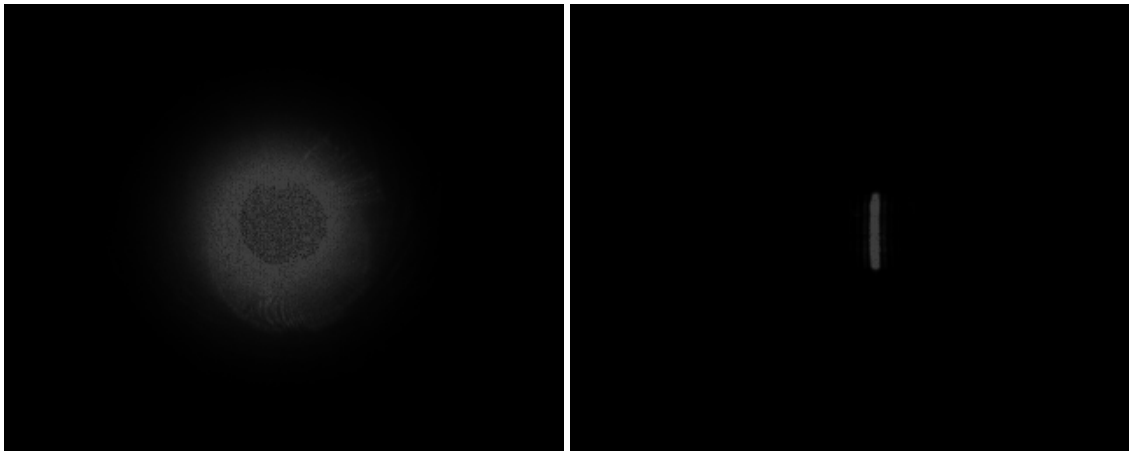

Figure 27: Collimated beam (left) and with mask in place (right).

3.4 Conclusion

Being a prototype instrument, the assembly process often required many new techniques to be considered. The optical bench alignment procedure had been partially formed during the breadboard instrument assembly, however this instrument was assembled at a different facility using different instruments. While there was some overlap in techniques that could be used, overall the procedures were relatively different. The telescope alignment procedure had spatial tolerances of less than 1 mm and did not allow for visual alignment. Added difficulty resulted from uncertain coupling between the telescope output facet and the slab waveguide input. Aligning the telescope also proved quite challenging using the IR beam while enclosed in the housing. Improvements could be made to this process through the use of additional laboratory equipment and better design of the housing to allow for partial visual alignment of the telescope.

4. CALIBRATION

4.1.1 Introduction

Calibrating methods for traditional spatial heterodyne spectrometer are well established (Englert & Harlander (2006); Englert et al., (2004)). The main difference between a SHS and FTS is that the interferogram of a FTS is recorded by a single detector whereas a SHS records all elements of the interferogram at a single time across a detector array (Englert & Harlander, 2006). This removes temporal source variations (Brault, 1988) eliminating brightness changes and timing errors within interferogram sampling. Inaccuracies existing within the SHS system result from fabrication errors within the waveguide, limitations on the assembly process and inherent non-uniformities residing within the detector itself. Performance details related to these imperfections individual waveguides are systematic errors and do not depend on the scene allowing errors to be corrected for during post data processing.

This section details the methods used to derive coefficients that will correct for aberrations within the mechanical and optical system detailing how the instrument differs from an idealized version. Coefficients which the system takes into account includes system errors that result from fabrication errors within the waveguide, limitations on the assembly process and inherent non-uniformities residing within the detector itself. An understanding of the spectrometer system as a whole allows these variations to be characterized and minimized through algorithms used in data analysis. The calibration process requires the waveguide to be characterized prior to being assembled in the spectrometer as well as the entire instrument post-assembly. The signal for each waveguide channel S_i can be written as:

$$S_i = G_i t\left[I_\circ t_i\left\{1 \pm M_i \cos\left(\frac{2pD_i(T)}{l}\right)\right\} + Id_i(T)\right] \qquad \textbf{Equation 5}$$

where G is the electronic gain, t is the integration time, I_o is the current, τ is the optical throughput of the channel, M is the modulation efficiency, L is the optical path difference of the MZI, $\boldsymbol{\lambda}$ is the wavelength, d is the dark current constant as a function of temperature and subscript i denotes the interferometer and pixel number. This equation was taken from internal documentation at COM DEV, and credit is given to Dr. Allan Scott. Quantities that need to be accurately calibrated are:

a. Dark Signal
b. Photo-Response Non-Uniformity
c. Path difference as a function of chip temperature
d. Modulation efficiency
e. Crosstalk

4.1.2 Dark Signal

The dark signal of the detector accumulates roughly linearly with time and also over small temperature regions, and should be quantified over the operating temperature range of the application at sufficient precision to meet the requirement. The temporal variability of the dark signal was measured over varying intervals in order to determine the necessity of recalibrations. From the above equation, the dark signal is:

$$G_i Id_i$$ **Equation 6**

An estimate of the gain was calculated using the lasers power and detector counts.

Table 4: Gain Parameter Values

Input strength	64 μW/(π*2.5mm^2) = 3.2611 μW/mm^2
Area of waveguide input	111 * 2um * 4 μm = 888 μm^2
Input power	0.0028959 μW*10μs = 2.896e^{-14} J
Integration time	10 μs
Total counts	147,200
Quantum efficiency	0.85
Photons received	173,176

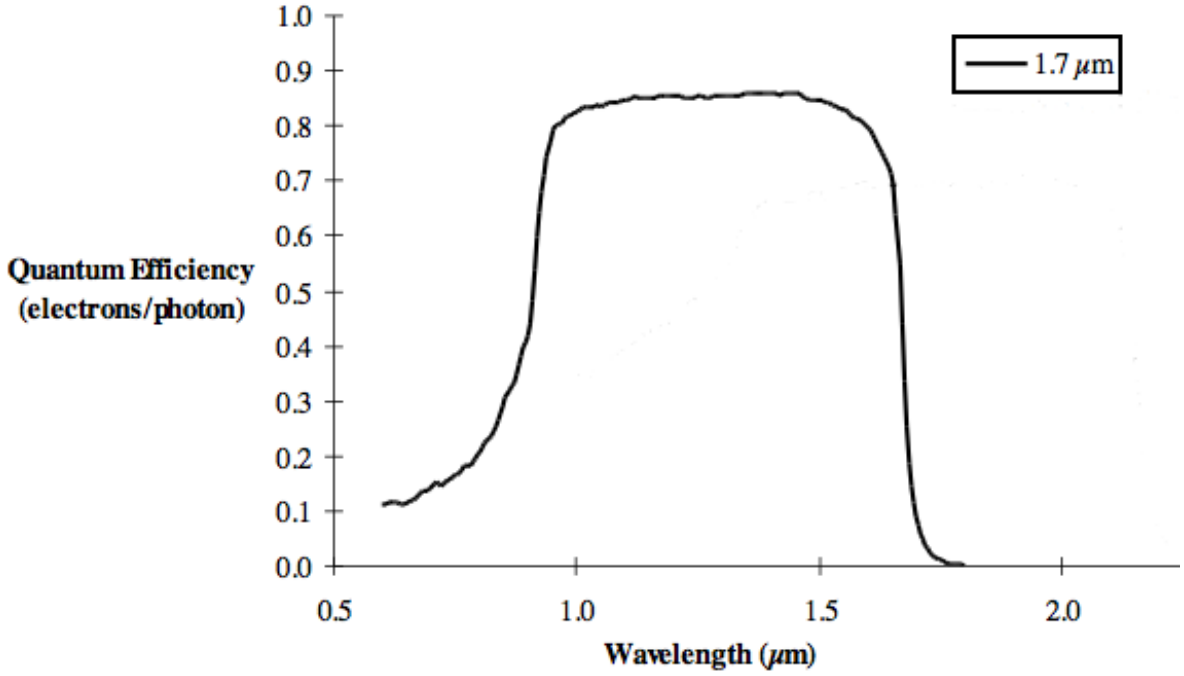

Figure 28: Quantum efficiency of the detector as a function of radiation wavelength. (credit: Sensors Unlimited)

Table 5: Gain Calculation

$\lambda = 1.36\ \mu m$

$E = hv$

$$\left(\frac{3.0\times10^{8}}{1.36\times10^{-6}}\right)\left(6.626\times10^{-34}\right) = 1.46161741\times10^{-19}$$

Therefore,

$$\left(\frac{2.89600\times10^{-14}}{1.46161741\times10^{-19}}\right) = 198136.666$$

$$Gain = \frac{173176}{1.98137} = 0.87402151$$

4.1.3 Photo-Response Non-Uniformity

Wavefront errors and contamination in the incoming optics provide variations in the uniformity of illumination. Errors in the waveguide and photo-lithographic processes can cause variations in the channel-to-channel throughput. Variations in the detector semiconductor properties cause differences in the quantum efficiency of photon detection. Variations in the electrical properties of the silicon readout IC create non-uniformities in the pixel output gains. Together these variations need to be characterized and removed to allow a low noise spectral inversion. From the above equation, the photo-response non-uniformity is:

$$G_i\tau_i \qquad \textbf{Equation 7}$$

The photo-response non-uniformity and modulation efficiency quantities can be determined by scanning a tunable laser over the system passband. A diffuse, expanded input should be used to fill the system étendue. By taking a series of frames at finely separated wavelengths throughout the passband, the cosine transform of each MZI will be traced out.

A linear least-squares fit of this sequence of (dark-subtracted) points to the best fit cosine wave was used to determine the frequency ($2\pi L_i$), the amplitude ($G_i t I_0 \tau_i M_i$), and the offset ($G_i t I_0 \tau_i + G_i t I_0 d_i$) for each waveguide. The results of several waveguide measurements are shown in **Figure 29** below.

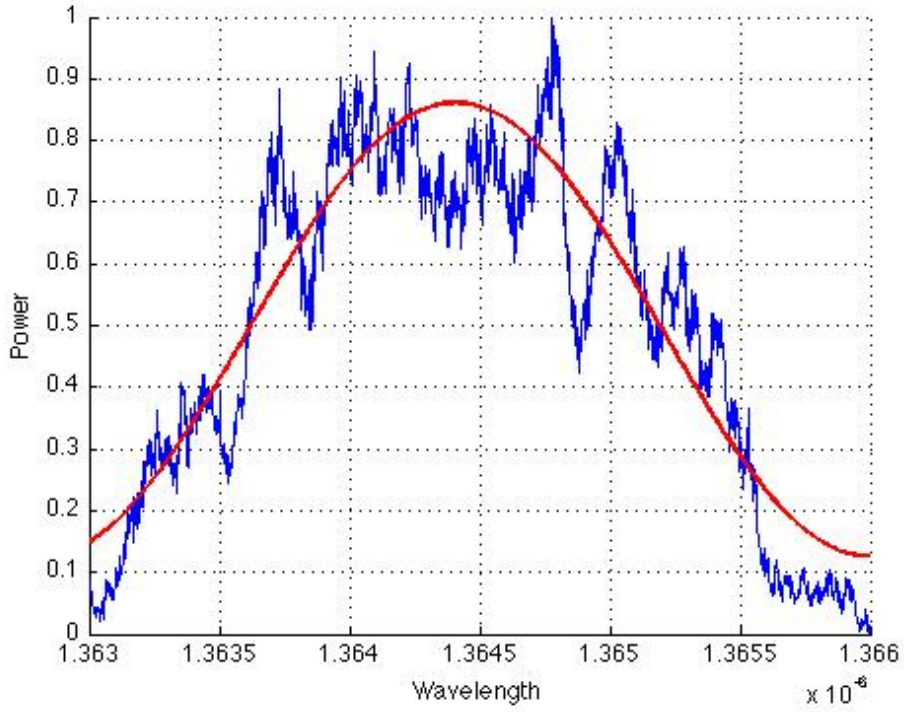
Power
Wavelength
x 10^-6
0
0.1
0.2
0.3
0.4
0.5
0.6
0.7
0.8
0.9
1
1.363
1.3635
1.364
1.3645
1.365
1.3655
1.366

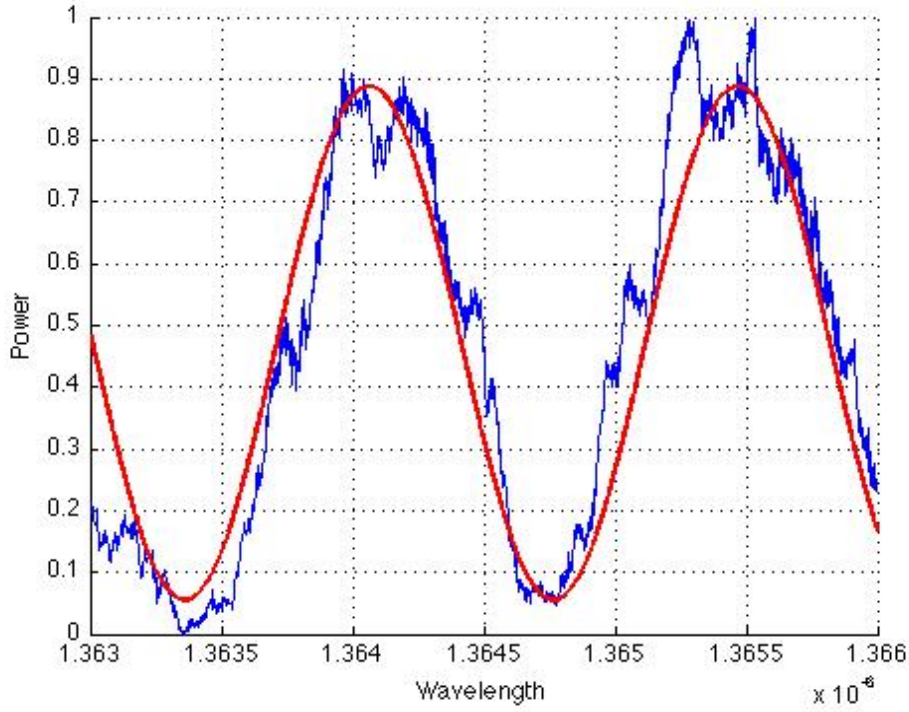
Power
Wavelength
x 10^-6
0
0.1
0.2
0.3
0.4
0.5
0.6
0.7
0.8
0.9
1
1.363
1.3635
1.364
1.3645
1.365
1.3655
1.366

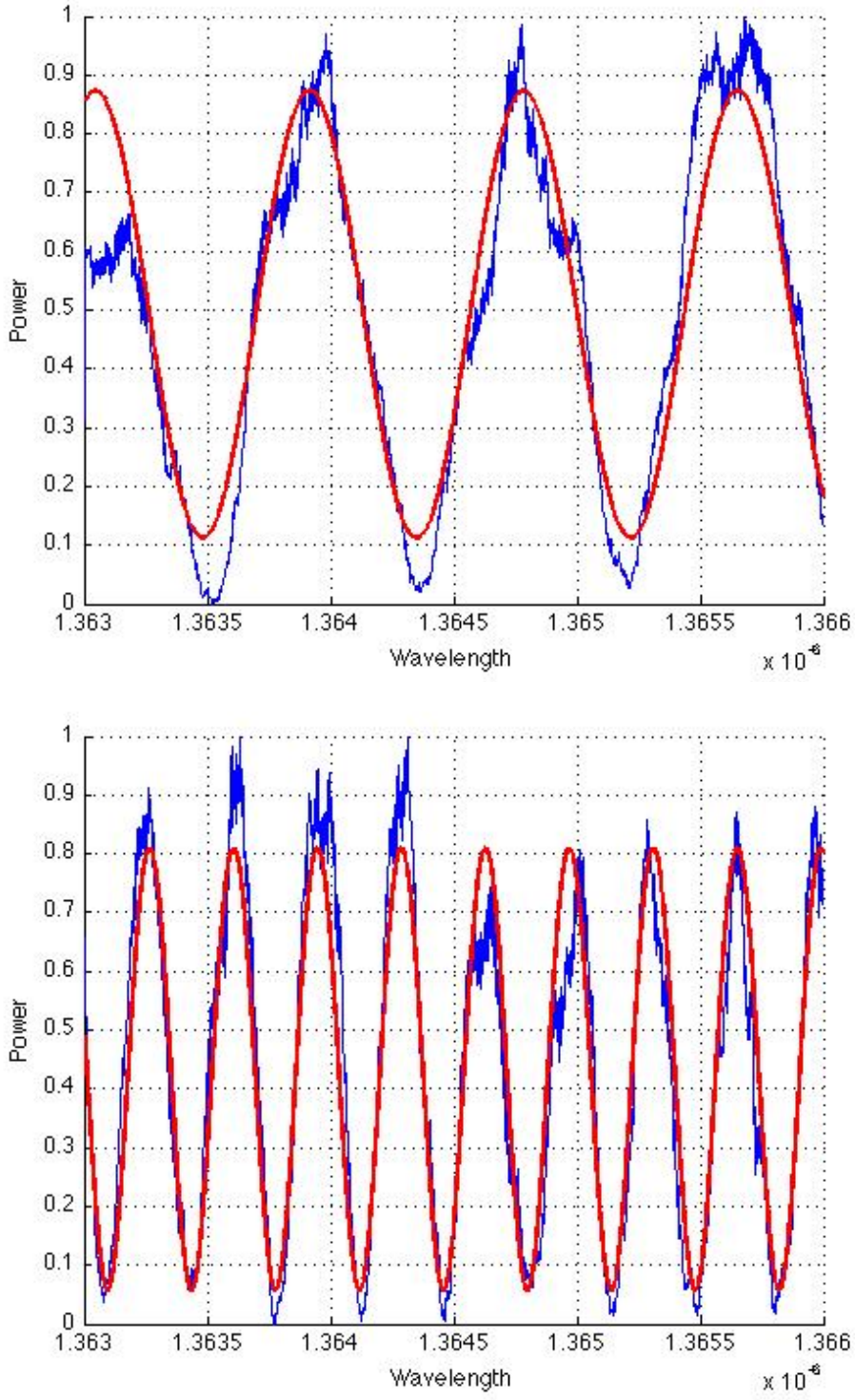

Figure 29: Fitting a cosine curve to the output of 4 MZI's.

For complementary outputs of each MZI, the measured frequencies should be averaged to provide a single path difference for the channel. By normalizing the offset of each output, the relative PRNU can be determined (assuming I_0t is constant). Finally, the modulation efficiency can be determined by dividing the amplitude by the offset for each channel. Again, the measured modulation efficiency should be averaged for each pair of complementary outputs.

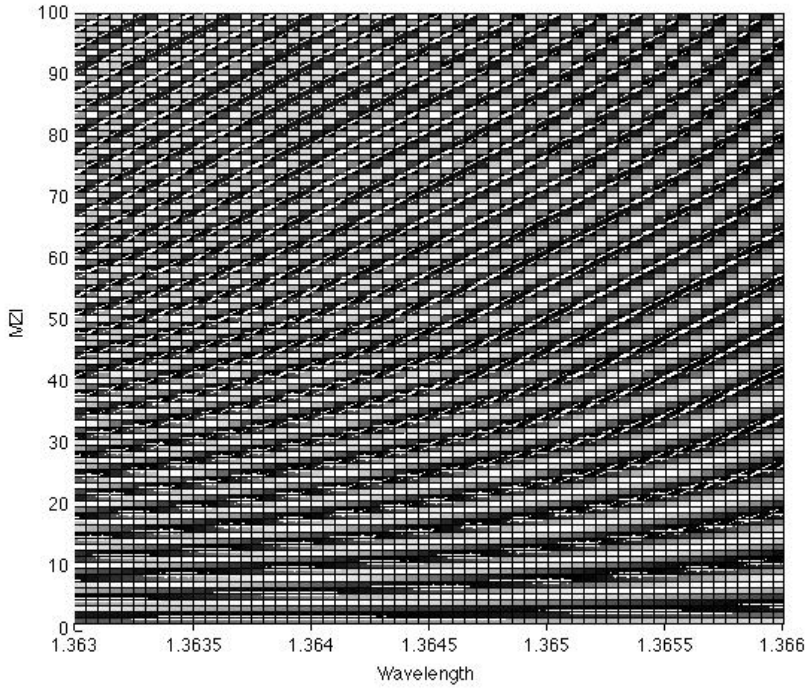

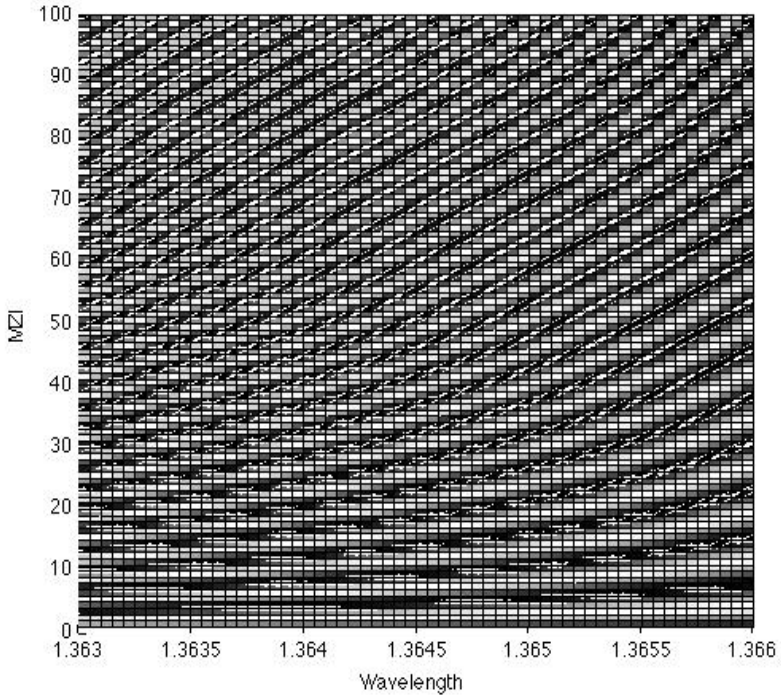

Figure 30: Simulating the output off all 100 MZI's with throughports (left) and cossports (right).

4.1.4 Path difference as a function of chip temperature

To be able to properly apply the Discrete Fourier Transform on the retrieved power interferogram, variations in the path length delay will need to be quantified. This is possible by maximizing a monochromatic laser source using the same method as in the previous procedure. This will allow the path length delay error to be found through the difference of the expected maximum power wavelength and the actual wavelength. This difference in wavelength will correspond to the path length error of the interferometer.

4.1.5 Modulation efficiency

Due to the fabrication of the waveguide, the input couplers may not split the input signal precisely in half. This effect may be measured and quantified by minimizing a monochromatic input signal using the same setup as the previous two procedures. Ideally, when the signal is minimized, the power should be zero due to complete destructive interference. However, if one interferometer arm contains more signal, when the two signals in each interferometer are recombined, some signal will still exist and a power will be detected. The magnitude of this power can alluded to uneven loses in the interferometer arms and an unequal splitting of the signal through the input coupler.

4.1.6 Crosstalk

Crosstalk between waveguide output facets and neighboring pixels is caused from alignment errors during assembly and an uneven output facet. By illuminating a single waveguide, it is possible to quantify this crosstalk allowing it to be subtracted from the power interferogram. This was done for each of the 211 outputs and the crosstalk expressed as a percentage of total signal is shown in **Figure 31** below.

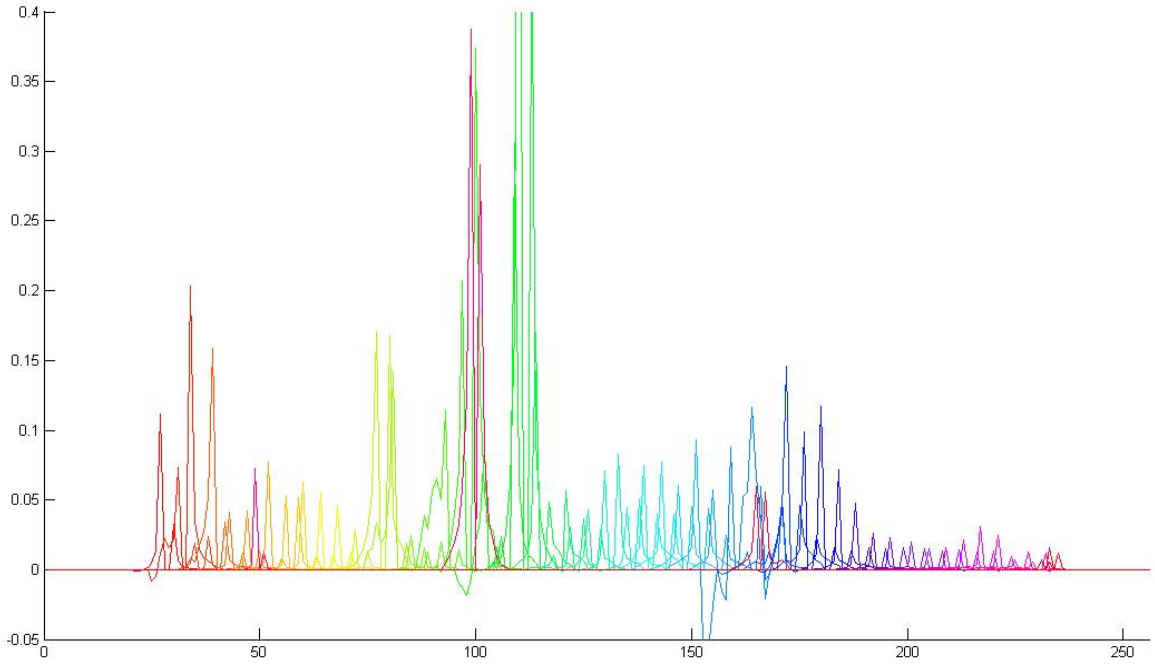

Figure 31: A normalized measurement of crosstalk between waveguides. (Horizontal axis is readout from respective detector pixel. Vertical axis is fractional power readout measured from peak power)

4.1.7 Humidity

For thoroughness, it is important to consider the humidity within the laboratory. During assembly and calibration, the humidity at the National Research Councils lab was not controlled, however in COM DEV's class 1000 clean room was held at a constant relative humidity of 30%. An absorption spectrum of the water vapor present at the National Research Council's lab is shown as a reference signal below. It can be seen that a decrease of up to 2 dB can be observed due to water vapor existing in the optical pathway of the beam. It is recommended that the calibration take place in an area with low humidity. The effect of ambient water vapor is shown below.

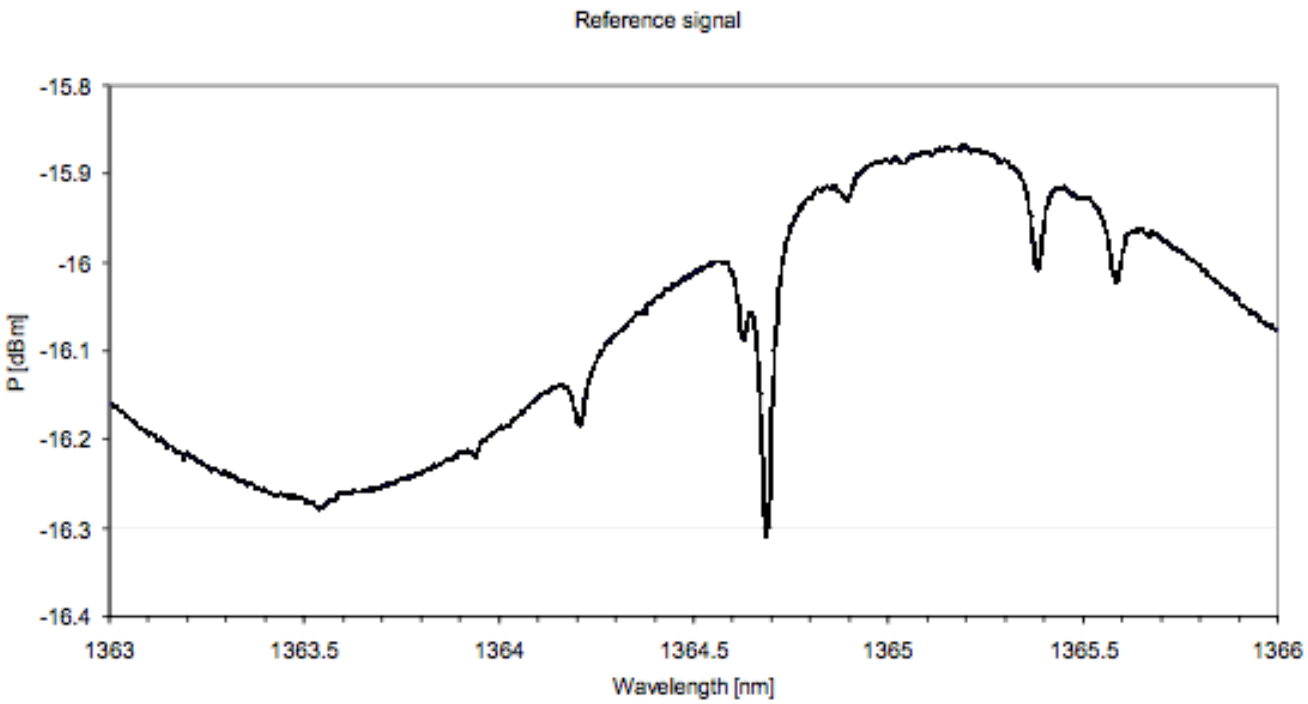

Figure 32: Reference spectrum showing water vapor absorption from humidity in laboratory air. This figure is meant for illustrative purposes and credit is to Mirek Florjańczyk and his work at the National Research Council.

5. INSTRUMENT SIMULATION

5.1 Introduction

The line-by-line radiative transfer code, GENSPECT, is used to compute all theoretical transmission functions (Quine et al., 2001). It features a selectable interpolation error tolerance, an instrument model and inversion routines for nadir and limb viewing configurations. The water vapor absorption spectrum was simulated over the 1363.25 nm to 1365.75 nm band using a limb viewing geometry with several tangent heights. The results of this are shown in **Figure 33** below.

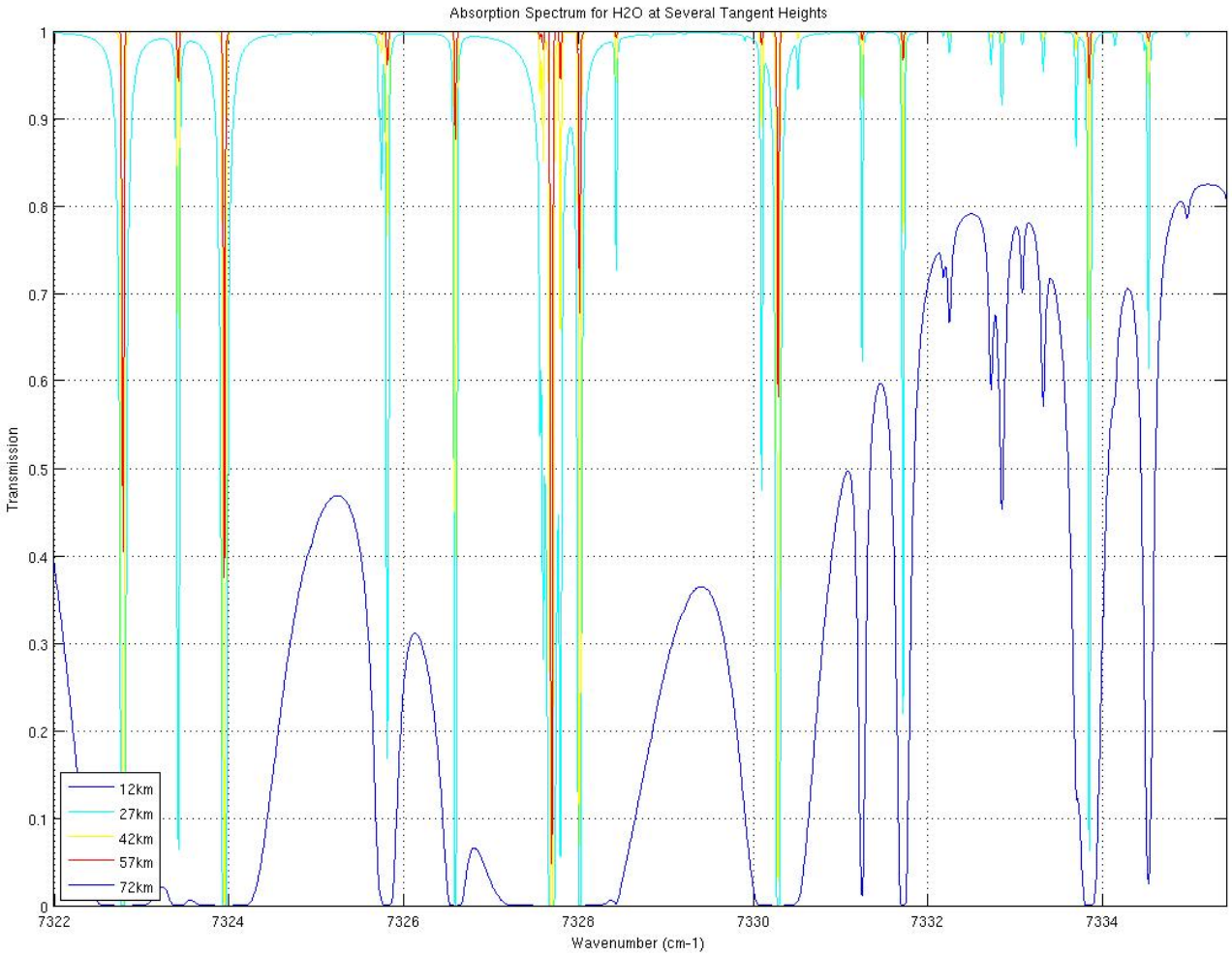

Figure 33: Simulated water vapor absorption spectra for several tangent heights.

5.2 Instrument Model

A mathematical model was created to simulate the instruments performance and used in retrieving the input spectrum. The instrument model uses a Littrow wavelength of 1364.5 nm over a 2.5 nm

spectral range, an effective index of refraction of 3.47 and implementing an array of 100 MZI's. Using the equation in **Equation 8** as a relation:

$$\delta\lambda = 2\frac{\Delta\lambda}{N_{\min}} \qquad \textbf{Equation 8}$$

Where $\Delta\lambda$ is the wavelength spectral range, N_{min} is the minimum number of sampling points and $\delta\lambda$ is the wavelength resolution, results in a wavelength resolution of 0.05 nm. A common resolution measurement for grating spectrometers is *resolving power* and is given by:

$$R = \frac{\lambda_\circ}{\delta\lambda} \qquad \textbf{Equation 9}$$

Where λ_o is the Littrow wavelength. Therefore, this spectrometer has a resolving power of 27 290. The maximum path length delay of the interferometer array is given by:

$$\Delta L_{\max} = R\frac{\lambda_\circ}{n_{eff}} \qquad \textbf{Equation 10}$$

Where n_{eff} is the effective index of refraction. From this, the maximum path length delay is 1.073 cm. An individual MZI is composed of an oscillatory term given by the cosine of the wavenumber and a constant background, it can be represented by:

$$T(\sigma) = \frac{P^{out}}{P^{in}} = \frac{1}{2}\left[A \pm B\cos\left(\frac{2\pi}{\lambda} n_{eff} \Delta L\right)\right] \qquad \textbf{Equation 11}$$

Where σ is the wavenumber, *A* and *B* are constants coefficients related to the MZI's physical structure (Florjańczyk et. al., 2011). From this equation and using the simulated atmosphere as input, the resulting power interferogram can be seen in **Figure 34**.

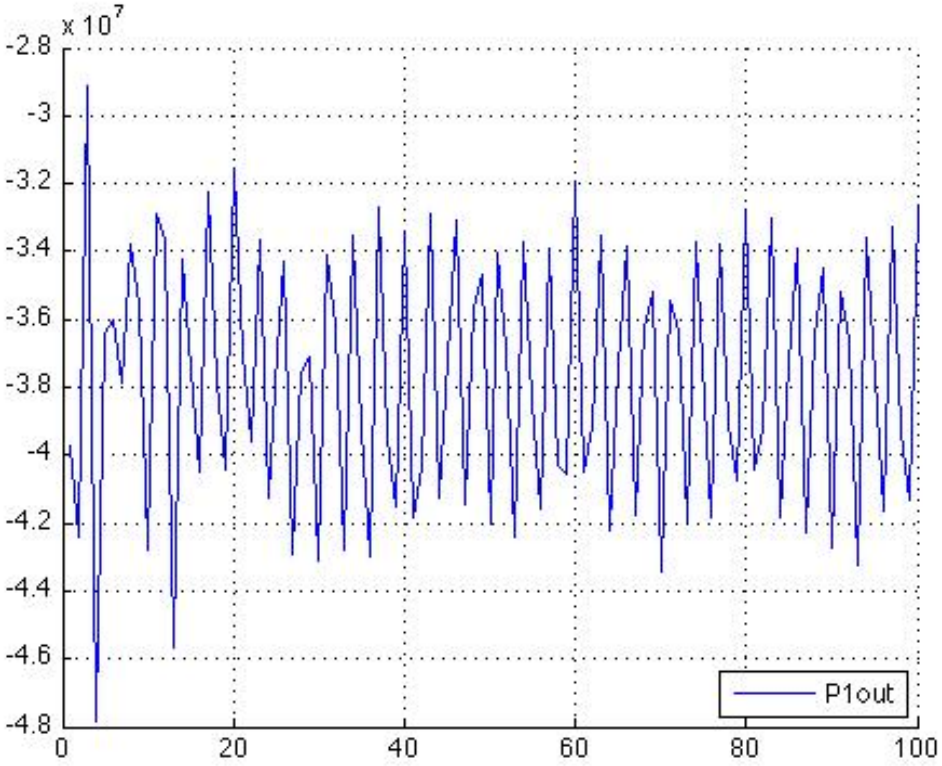
x 10^7
-2.8
-3
-3.2
-3.4
-3.6
-3.8
-4
-4.2
-4.4
-4.6
-4.8
0
20
40
60
80
100
P1out

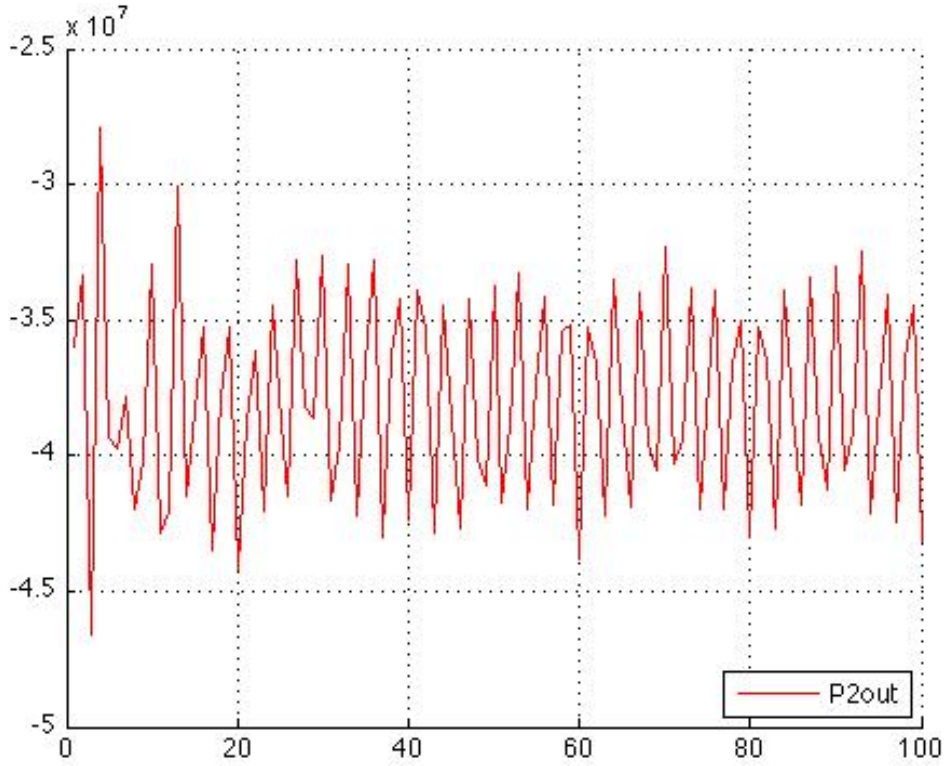

Figure 34: Power interferogram of the input function for throughports (blue) and crossports (red).

The output of the MZI array is a discrete Fourier transform of the input signal. By applying a Fourier transform to the interferogram (P^{out}) the input spectrum can be calculated as:

$$p^{in}(\bar{\sigma}) = \frac{n_{eff}\Delta L_{\max}}{N} P^{in} + 2\frac{n_{eff}\Delta L_{\max}}{N}\sum_{i=1}^{N} W(x_i)F(x_i)\cos 2\pi\bar{\sigma}x_i \qquad \textbf{Equation 12}$$

Where $\bar{\sigma}$ is the modified wavenumber, P^{in} is the input power into each interferometer, $W(x_i)$ is the apodization function, and:

$$F_i = -\frac{1}{B_i}\left(2P^{out}\left(x_i\right) - A_i P^{in}\right)$$ **Equation 13**

This results in the retrieved interferogram **Figure 35** (Florjańczyk et. al., 2011). The recovered spectrum is apodized, which would decrease resolving power but would remove artifacts.

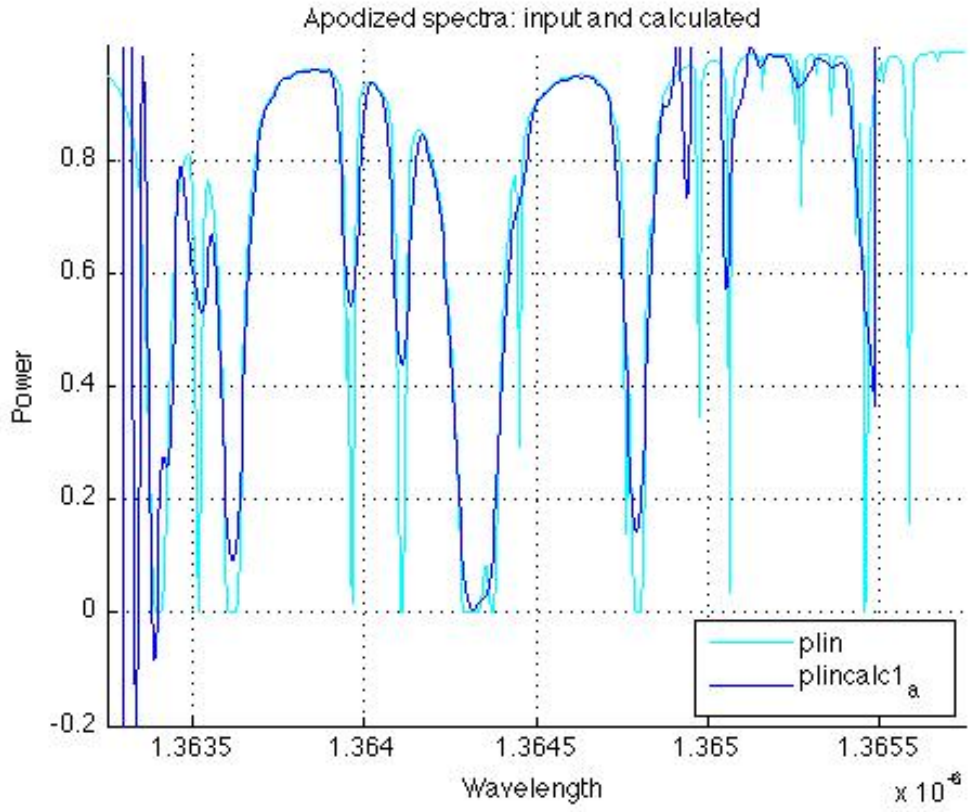

Figure 35: The input spectrum(cyan) and calculated input spectrum (blue).

5.3 Conclusion

When the input spectrum is compared to the calculated spectrum, some spectral features are lost. Notably, the deep and narrow absorption lines are less evident in the calculated spectrum, and some of the neighboring absorption lines are amalgamated into some irregularly shaped absorption lines in the calculated spectrum. This is due to features finer than the Rayleigh resolution not being able to be resolved.

6. SAMPLE RETRIEVAL

6.1 Introduction

An example retrieval of a monochromatic input signal is shown in the proceeding section. The data processing and correction algorithm was developed using the calibration methods described above, as well as other post processing steps including:

a. Data averaging
b. Dark Signal Subtraction
c. Waveguide crosstalk subtraction
d. Waveguide Pair Gain Correction
e. Photo-Response Non-Uniformity
    a. Normalization
    b. Pixel Removal
    c. Interpolation

f. Pixel Reorder

g. Fast Fourier Transform (FFT)

6.2 Data averaging & Dark Signal Subtraction

Before any transformation can be applied to the interferogram, a dark frame is subtracted from the raw interferogram. Background signal varies with the detector temperature and background light, however, the general shape of the background signal remains constant, only varying in strength. This allows the acquired dark frame to be fitted through a linear least squares method to each frame. Based on an analysis of the expected random noise, the dark signal was averaged over ~100 master frames. The dark frames are measured by covering the input so that no light can enter the waveguide. This high signal to noise dark signal measurement will then be subtracted from the raw data for each of the subsequent calibrations. The dark frames were averaged while the source was held constant. The resulting interferogram is shown in **Figure 36**.

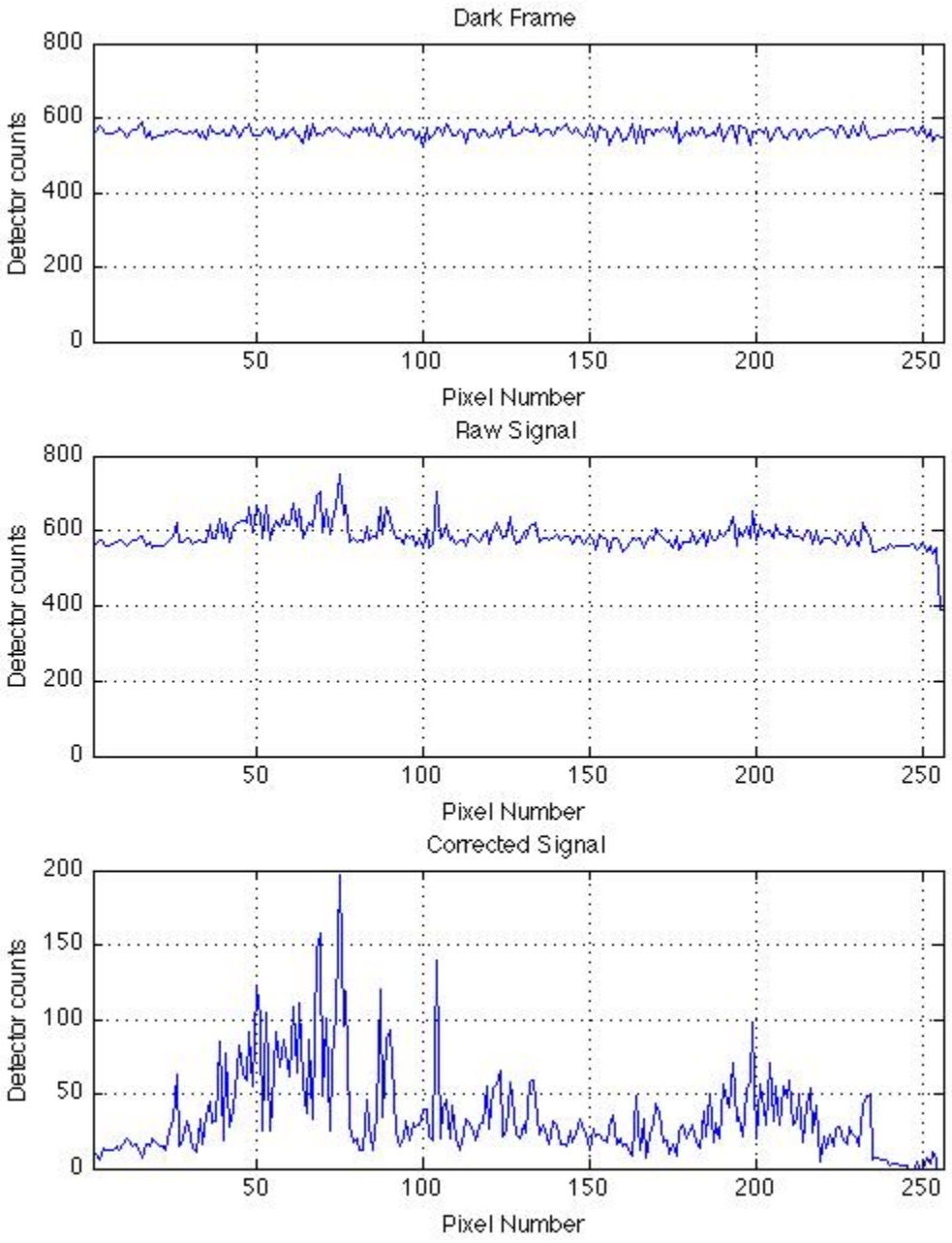

Figure 36: The dark frame (top), signal (middle) and the dark frame subtracted signal (bottom).

6.3 Waveguide crosstalk subtraction

The interpixel spillage correction subtracts cross talk between neighboring waveguides. Quantification of waveguide crosstalk was measured during the assembly process, when individual interferometers were illuminated using an optical fiber, and the resulting output was recorded.

The 211 unknown variables representing the input signal to each channel are found through matrix inversion technique where $A = C^{-1}B$ is used as a solution to $C = AB$. C is a vector representing each output port of the slab and C is a matrix containing all of the pixel spillage information. B is a vector representing the actual signal input to each interferometer.

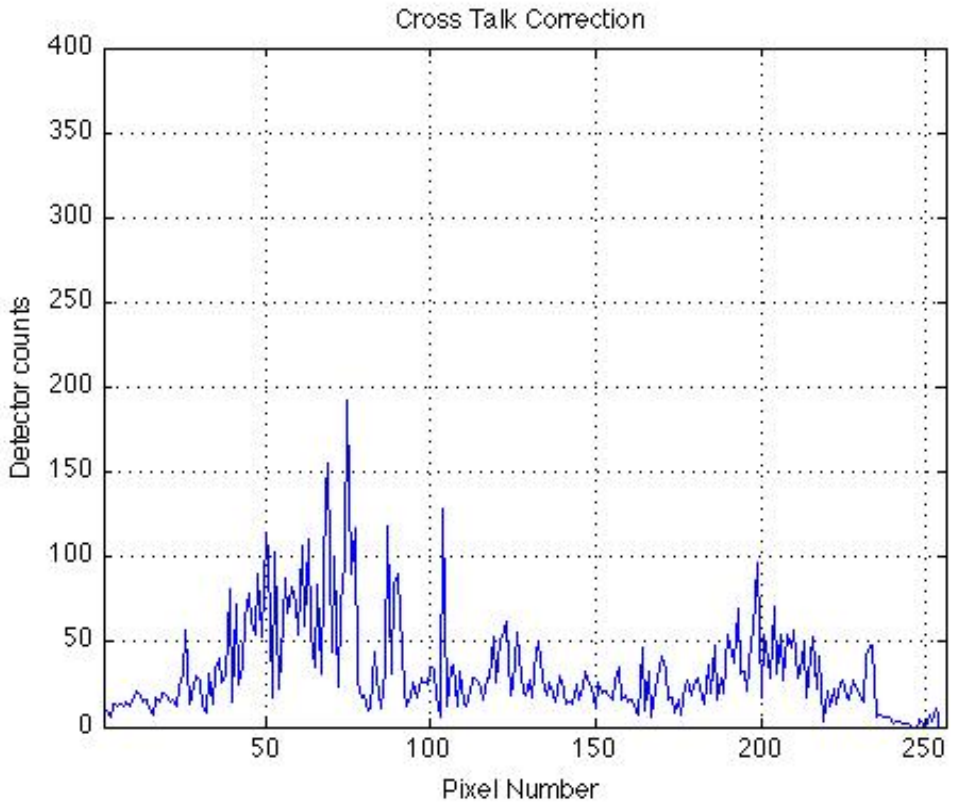

Figure 37: The resulting frame after pixel cross talk was removed..

6.4 Waveguide Pair Gain Correction

The waveguide pair gain correction is required to correct for coupling and throughout variations in the waveguide. It is applied by summing corresponding throughports and crossports and normalizing each arm of the interferometer by the same normalization constant.

6.5 Photo-Response Non-Uniformity

Two methods were used to correct for photo-response non-uniformity. The first is a normalization procedure and the second involves removing inaccurate pixels and using an interpolation procedure.

a. Normalization

This approach corrected signal strengths by referencing monitoring waveguide signal strength. The approach is based on equal signal strength of the monitoring waveguides. This is shown in **Figure 38** below.

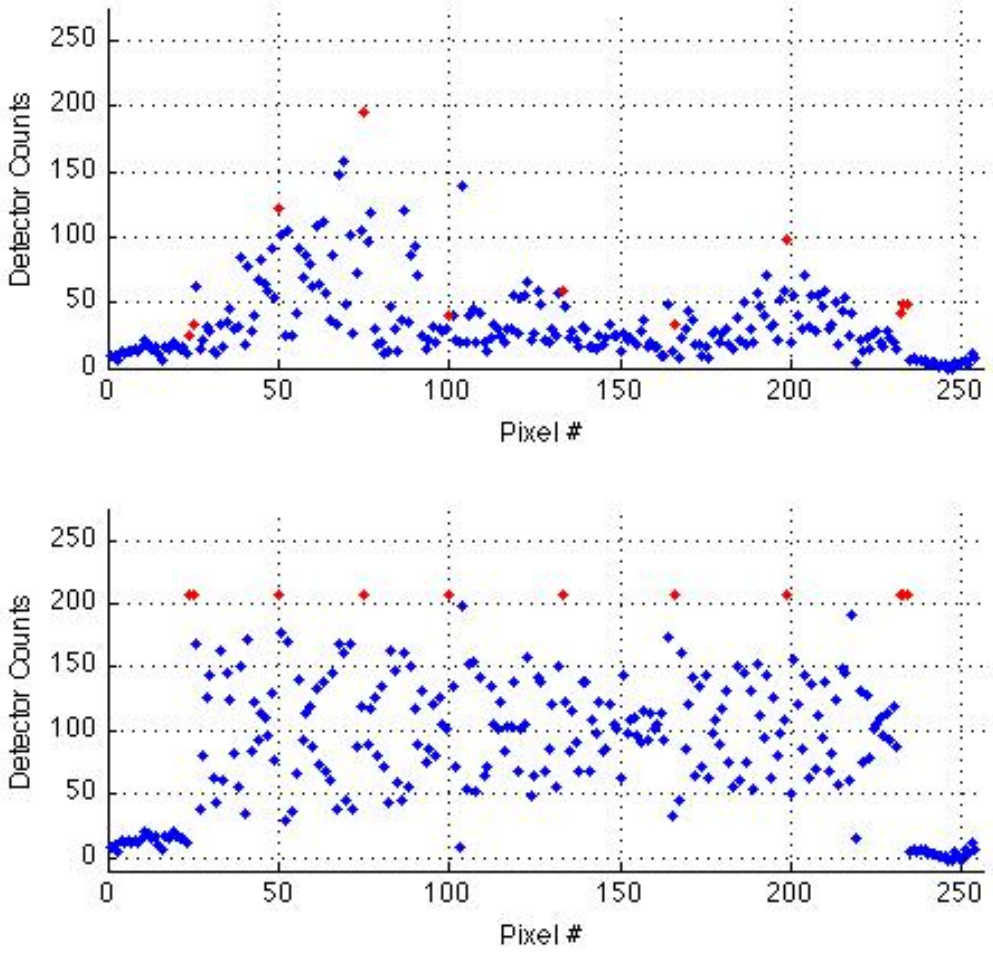

Figure 38: Normalization

b. Pixel Removal

This approach uses the interpixel spillage table to identify pixels with threshold errors. In this case, 6 pixels were found to have more than 25% error with 5 waveguides causing this error. The output from these pixels were removed from the interferogram and a spline interpolation

was used after the waveguides were reordered in terms of path length delay. This is shown in **Figure 39** below.

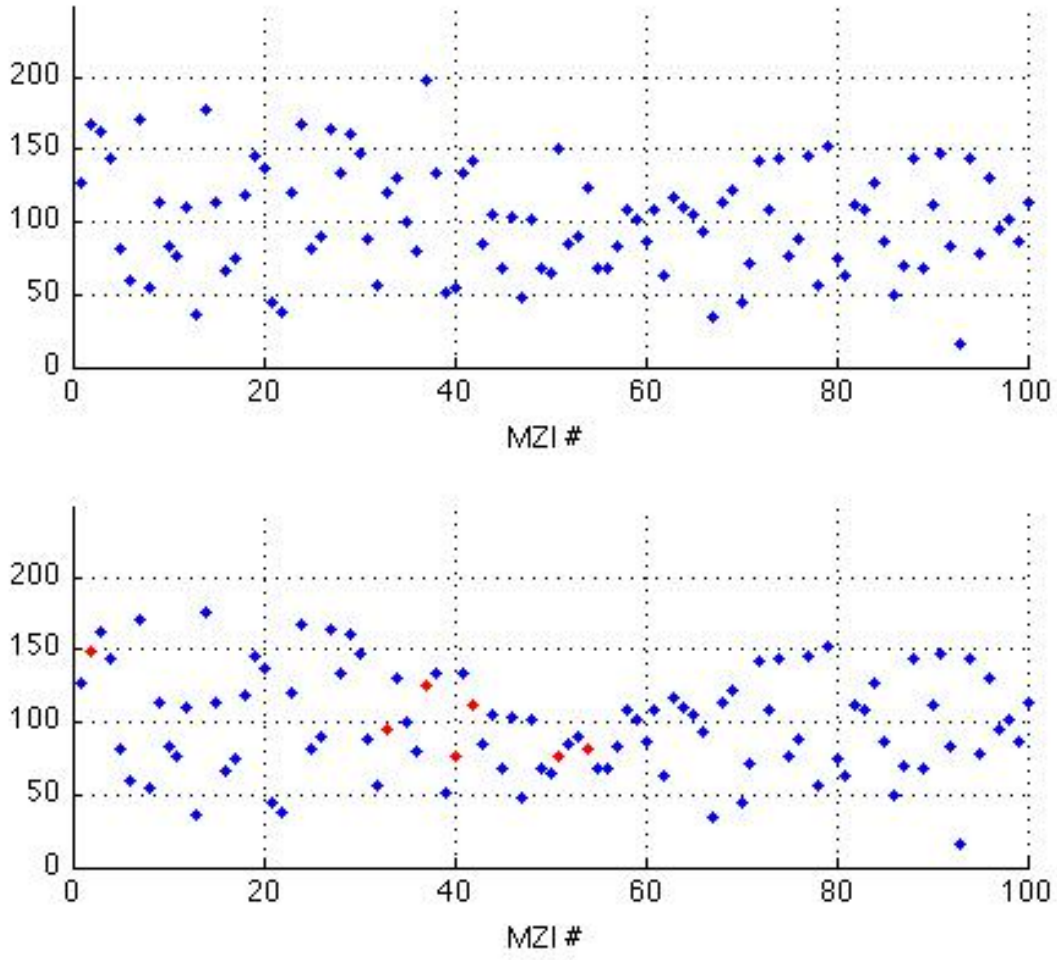

Figure 39: Pixel Removal and interpolation

6.6 Fast Fourier Transform

The Discrete Fourier transform is applied to the interferogram revealing the input spectrum. The output power interferogram can be changed into the input spectrum through the use of the Discrete Fourier Transform. The result from this is shown in **Figure 40** and **Figure 41** below.

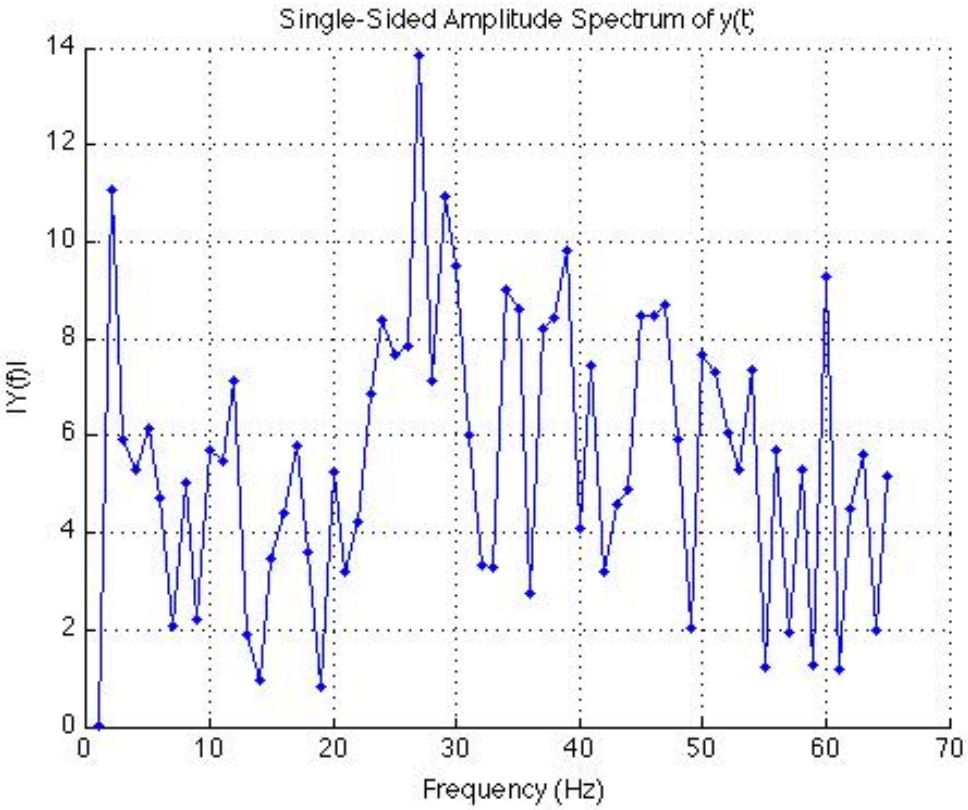

Figure 40: Throughport retrieval

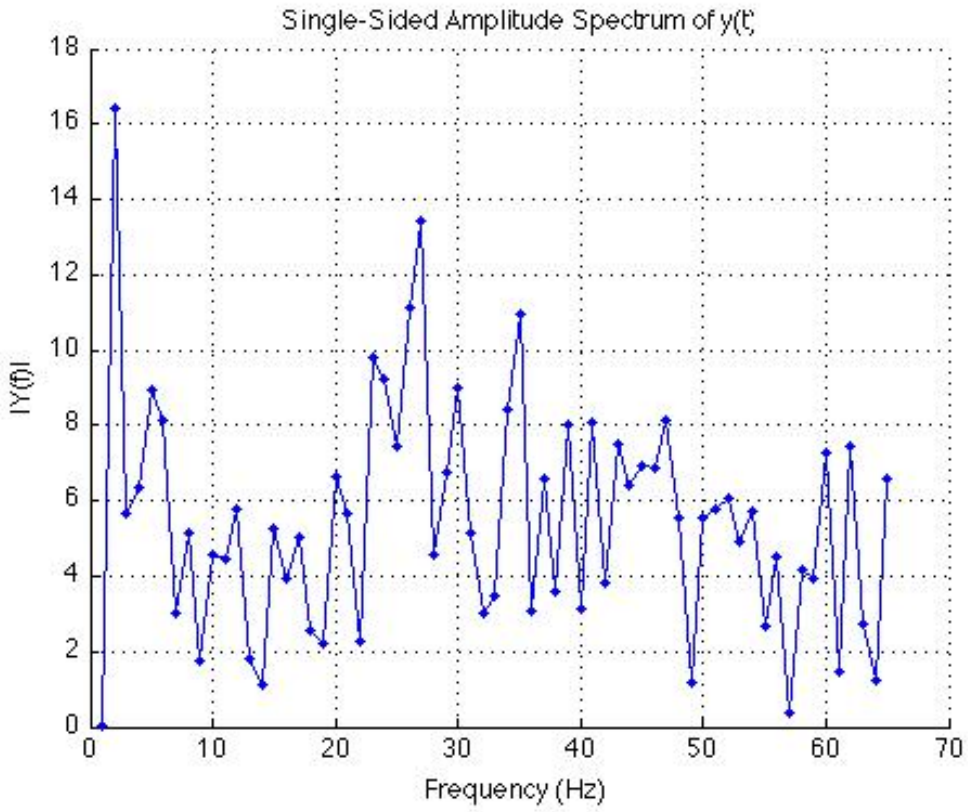

Figure 41: Crossport retrieval

6.7 Conclusion

The retrieved signal contains a lot of noise although a noticeable increase in signal in the center of the spectrum could correspond to the monochromatic laser input. This is likely due to the interpixel spillage correction algorithm not removing all of the interpixel crosstalk. Improvements could be made by better characterizing the interpixel spillage and using this in the algorithm.

7. CONCLUSION

The design, assembly, calibration, instrument modeling and a sample retrieval was presented. The broad function of the instrument is to format light for the waveguide, provide a spatially stable environment for the slab waveguide and have an output interface.

The hardware design of the instrument was effective in achieving the broad overall goals. The design also accounted for the complicated assembly procedure required for such a device. For instance, the alignment of the lenses in the telescope system was considered.

A higher level design aspect of the slab-waveguide itself would benefit from preventing it from propagating signal at the waveband of interest. This was a fundamental limitation and drawback in being able to distinguish signal from background noise and had negative effects during alignment, calibration and testing the instrument.

Improvements could be made to the overall size and more so the weight of the instrument, both the optical bench and telescope mount could have their mass reduced without sacrificing performance. The communication of the instrument did implement all required functions, however did not implement all aspects initially discussed, such as onboard processing of data.

Being a prototype instrument, the assembly process often required many new techniques to be considered. The optical bench alignment procedure had been partially formed during the breadboard instrument assembly, however this instrument was assembled at a different facility using different

instruments. While there was some overlap in techniques that could be used, overall the procedures were relatively different. The telescope alignment procedure had spatial tolerances of less than 1 mm and did not allow for visual alignment. Added difficulty resulted from uncertain coupling between the telescope output facet and the slab waveguide input.

Calibrating the instruments performance was completed using a variety of well-documented methods. The dark signal, photo-response non-uniformity, path difference as a function of chip temperature, modulation efficiency and crosstalk were all characterized. Improvements could be made to the accuracy of the crosstalk characterization.

The mathematical model of the instrument was designed to simulate the instrument's performance and used in retrieving the input spectrum. The model itself was used to test the theoretical performance of the instrument. When the input spectrum was compared to the calculated spectrum, it could be seen that some spectral features were lost. Improvements could be made to the automation of the process. Currently several large programs are required to simulate a single output.

A sample retrieval concluded the main section and was performed using the characterization techniques and instrument model. The retrieved signal was observed to contain noise resulting from the interpixel spillage correction algorithm not removing all of the interpixel crosstalk.

8. REFERENCES

1. Brault, J. W., "High precision Fourier transform spectrometry," Mikrochim. Acta (Wien) 1987 III, 215-227 (1988).
2. Cheben, P., [Optical Waveguides: From Theory to Applied Technologies], CRC Press, London, Chapter 5 "Wavelength dispersive planar waveguide devices: Echelle gratings and arrayed waveguide gratings", (2007).
3. Dessler, A. E., Z. Zhang, P. Yang, Geophys. Res. Lett. 35, L20704 (2008).
4. Englert, C. R., J. M. Harlander, J. G. Cardon, and F. L. Roesler (2004), Correction of phase distortion in spatial heterodyne spectroscopy, Appl. Opt., 43, 6680–6687.
5. Englert, C. R., and J. M. Harlander (2006), Flatfielding in spatial hetero- dyne spectroscopy, Appl. Opt., 45, 4583–4590.
6. Florjańczyk, M., P. Cheben, S. Janz, A. Scott, B. Solheim, and D.-X. Xu, "Multiaperture planar waveguide spectrometer formed by arrayed Mach-Zehnder interferometers," Opt. Expr. 15(26), 18176-18189 (2007).
7. Florjańczyk, M., P. Cheben, S. Janz, A. Scott, B. Solheim, and D.-X. Xu, "Planar waveguide spatial heterodyne spectrometer," Proc. SPIE 6796, 6796-81 (2007).
8. Florjańczyk, M., P. Cheben, S. Janz, A. Scott, B. Solheim, and D.-X. Xu, "Spatial heterodyne planar waveguide spectrometer: theory and design", Proc. SPIE 7099, 7099-43 (2008).
9. Florjańczyk, M., P. Cheben, S. Janz, B. Lamontagne, J. Lapointe, A. Scott, K. Sinclair, B. Solheim, and D.-X. Xu, "Multiaperture Fourier spectrometers in planar waveguides", Proc. SPIE 7812, 7218-42 (2009).
10. Florjańczyk, M., P. Cheben, S. Janz, B. Lamontagne, J. Lapointe, A. Scott, B. Solheim, and D.-X. Xu, "Slab waveguiode spatial heterodyne spectrometers for remote sensing from space,"

Optical sensors 2009. Proceedings of the SPIE, Volume 7356 (2009)., pp. 73560V-73560V-7 (2009).

11. Florjańczyk, M., Bock, P., Lamontagne, B., Cheben, P., Ramos, C.A., Ortega-Moñux, A., Halir, R., Fernandez, I.M. (2011). Slab waveguide spatial heterodyne spectrometer for SHOW application. Final Report. Institute for Microstructural Sciences National Research Council Canada.
12. Forster, P. et al. in IPCC Climate Change 2007: The Physical Science Basis(eds) Solomon, S. et al.) 129–234 (Cambridge Univ. Press, 2007)
13. Harlander, J., R. J. Reynolds, and F. L. Roesler, "Spatial heterodyne spectroscopy for the exploration of diffuse interstellar emission lines at far-ultraviolet wavelengths," Astrophys. J. 396, 730-740 (1992).
14. Kramer, H. J., "Observation of Earth and Its Environment – A Survey of Missions and Sensors," 51-61, Springer-Verlag, Berlin, 2002.
15. Lin, Y., G. Shepherd, B. Solheim, M. Shepherd, S. Brown, J. Harlander, and J. Whiteway, "Introduction to spatial heterodyne observations of water (SHOW) project and its instrument development," in Proc. XIV Int. TOVS Study Conf., 25-31 May 2005, Beijing, China, 835-843 (2005).
16. Pachauri, R. K. & Reisinger, A. (eds) Climate Change 2007: Synthesis Report (Intergovernmental Panel on Climate Change, Cambridge, UK, 2007).
17. Quine, B. M., J. R. Drummond (2001) GENSPECT: A line-by-line code with selectable interpolation error tolerance.
18. Robertson, B., Scott, A., Norman, R. (2010a). Slab Waveguide Spatial Heterodyne Spectrometer Coupling Study. Field Programmable Gate Array Detailed Design Review.

COM DEV Ltd. Ottawa, Ontario.

19. Robertson, B., Scott, A. (2010b). Slab Waveguide Spatial Heterodyne Spectrometer Coupling Study. Preliminary Design Report. COM DEV Ltd. Ottawa, Ontario.
20. Robertson, B., Scott, A. (2010c). Slab Waveguide Spatial Heterodyne Spectrometer Coupling Study. System Requirements. COM DEV Ltd. Ottawa, Ontario.
21. Robertson, B., Scott, A. (2010d). Slab Waveguide Spatial Heterodyne Spectrometer Coupling Study. Design Development Plan. COM DEV Ltd. Ottawa, Ontario.
22. Robertson, B., Scott, A., Piche, L., Norman, R. (2011). Slab Waveguide Spatial Heterodyne Spectrometer Coupling Study. External Interface Control Document - Electronics. COM DEV Ltd. Ottawa, Ontario.
23. Scott, A., N. Rowlands, and A. Bell, "Miniature spectrometers for planetary remote sensing", Proc. SPIE 5660, 78-87 (2004).
24. Scott, A., M. Florjańczyk, P. Cheben, S. Janz, B. Solheim, and D.-X. Xu, "Micro-interferometer with high throughput for remote sensing." MOEMS and Miniaturized Systems VIII. Proceedings of the SPIE, Volume 7208 (2009)., pp. 72080G-72080G-7 (2009).
25. Scott, A., M. Florjańczyk, P. Cheben, S. Janz, B. Solheim, and D.-X. Xu, "Micro-interferometer with high throughput for remote sensing", Proc. SPIE 7208, 7208-18 (2009).
26. Sinclair, K., Benari, G., Saqur, R., Bar, O. (2009). Critical Design Report, The Micro Spectrometer Project. COM DEV Ltd. Ottawa, Ontario.
27. Trenberth, K.E., J. Fasullo, and L. Smith, 2005a: Trends and variability in column integrated atmospheric water vapor. Clim. Dyn., **24**, 741␣758.
28. Trenberth, K.E., P.D. Jones, P. Ambenje, R. Bojariu, D. Easterling, A. Klein Tank, D. Parker, F. Rahimzadeh, J.A. Renwick, M. Rusticucci, B. Soden and P. Zhai, 2007: Observations: Surface

and Atmospheric Climate Change. In: Climate Change 2007: The Physical Science Basis. Contribution of Working Group I to the Fourth Assessment Report of the Intergovernmental Panel on Climate Change [Solomon, S., D. Qin, M. Manning, Z. Chen, M. Marquis, K.B. Averyt, M. Tignor and H.L. Miller (eds.)]. Cambridge University Press, Cambridge, United Kingdom and New York, NY, USA.

9. APPENDICES

9.1 Appendix A: Waveguide-Sleeve Bonding

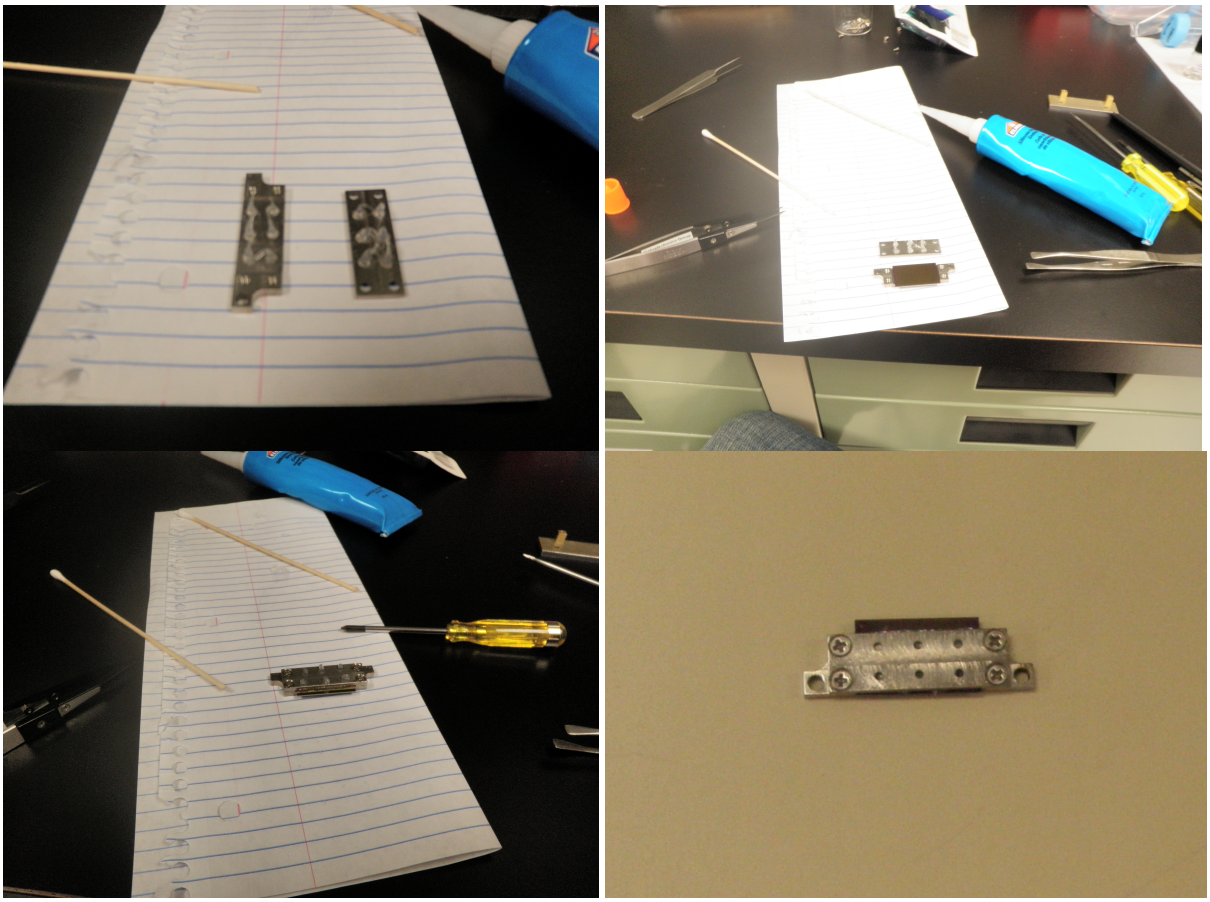

9.2 Appendix B: Optical Bench Alignment Procedure

Equipment Required:

2 tri-axis micropositioners
1 tri-axis micropositioners with yaw control
Tunable laser
Tapered fiber
Mounting equipment (figure 2)
Waveguide, detector and drive electronics
Circulator:

Positioner Setup:

1. Arrange three tri-axis positioners linearly so that they are sufficiently close to interact

with one another. Note that if only one of the positioners has rotational capability, ensure that it is placed in the center.

2. Loosely attach optical bench to an end positioner.
3. Loosely attach sleeve mount as well as sleeve to center positoner.
4. Loosely attach optical fiber to the remaining positoner.
5. Attach each of the three tri axis positioners to the optical table so that the fiber, waveguide, sleeve mount and optical bench can be aligned using their micrometer positioning knobs.
6. Remove optical bench, and sleeve mount from positioners.

Optical Bench Setup:

1. Visually align detector within the optical bench so that the pixels are approximately horizontal and located slightly above the center position of the sleeve cutout. Note, this offset is required because the waveguides are located near the top of the waveguide and not in its center.
2. Fasten the detector to the optical bench.
3. Attach the optical bench to its respective positioner.
4. Attach electronic hook up to the detector.

Attaching Waveguide to Sleeve:

1. Ensure that the position of the waveguide within the sleeve will allow enough overhang to allow the waveguide to have contact with the detector. (approximately 2-3mm)
2. Put several drops of silicon on the top and bottom of the sleeve near the holes.
3. Place waveguide upside down on the top half of the sleeve.
4. Place top half of sleeve onto bottom half and gently screw halves together.
5. Remove excess silicon which came through the holes in the sleeve.
6. Allow 30min for drying.

Marking Pixel/ Waveguide Positions:

To allow the position of the pixels and waveguide output positions to be available once the waveguide sleeve is inserted into the optical bench, marking must be made on the sleeve as well as the face of the optical bench to allow this.

1. Place sleeve (containing the slab waveguide) under microscope and mark beginning and ending positions of waveguide outputs on the opposite face (the face that will be exposed once the sleeve is inserted into the optical bench).
2. Repeat similar exercise with optical bench containing detector.

Positioning Waveguide with Detector:

1. Remove sleeve mount form central postioner.

2. Attach the sleeve to sleeve mount.
3. Attach sleeve mount to central positioner back a single hole position from the front most. (this is to align the z axis or yaw of the waveguide with the front edge of the optical bench)
4. Use microscope to adjust the yaw on the central positioner so that the front edge of the waveguide is aligned with the front edge of the optical bench.
5. Reattach sleeve mount with sleeve to front most hole on central positioner.
6. Couple the fiber input with a single monitoring waveguide on the chip.
7. Use the positioner with the optical bench to approach the waveguide while monitoring the power received by the detector.
8. Stop advancing the optical bench once the power is received by no more than 2 pixels.
9. If 2 pixels are receiving power the detector needs to be repositioned.

Adjusting Detector Position:

1. Move detector off the waveguide by at least 50 um (remember this value).
2. Move detector side to side estimating required movement from illuminated pixels and keeping in mind the detectors pixels are 50 um apart.
3. Bring detector forward again by same value used in step 1.

Repeat as necessary.

9.3 Appendix C: Communication

9.3.1 Introduction

Communication from the host PC to the SWISH spectrometer is implemented through a USB interface. The USB interface is used to download commands and parameters to the FPGA and to upload house keeping and status telemetry to the host computer. The following details a comprehensive description of requirements, background information, features and implementation techniques used by the host PC to interface with the SWISH spectrometer. Each relate to commands and telemetry, calibration, analysis and data storage.

9.3.2 Background

Data received from the spectrometer will include the Fourier transform of the interferometer data, two values for each interferometer in the array and the temperature of the detector. The Fourier transformed data received from the instrument can be considered the primary data while the data received in calibration mode can be considered secondary. Features of the GUI will include start, stop and reset buttons. A panel allowing the camera view displaying the data to be manipulated.

Onboard data analysis requires calibration coefficients being sent to the instrument. The coefficients will correct for aberrations within the mechanical and optical system. These coefficients the system will need to take into account will include from errors associated with the waveguide will include losses from the signals free space coupling to the waveguide, modulation efficiency of the input couplers within the waveguide as well as non-ideal path length delays of interferometers within the slab waveguide. Further, losses at the waveguide-detector interface will result from uneven alignment and coupling of the output signal from waveguide with detector pixels. More standard coefficients will include the derivation of a dark signal coefficient as well as a photo-response non-uniformity coefficient. These coefficients will need to be stored within the software and also be capable of being sent to the spectrometer for use in its spectrum retrieval algorithms.

The FPGA will have two main operational modes, characterization mode and spectral analysis mode. In characterization mode the FPGA simply sums/averages the pixels from multiple frames read from the photo array. In Spectral analysis mode the FPGA performs spectral analysis (including numerous corrections) on each frame read from the photo array and then sums/averages the resulting frequency bins over multiple frame periods. The FPGA the sends the time stamped results from the

sum/average process to the host computer via a USB interface. The onboard FPGA is from the Actel ProASIC3L line and is a A3P1000L device in the PQ208 Industrial Grade package. This is the FPGA that is used in all of the communication between the host PC and the instrument.

9.3.3 Requirements

The communication interface should be capable of reading and writing various commands to the instrument as per the External Interface Control Document (appendix IV). The communication interface is used for controlling and monitoring the internal electronics of the SWISH spectrometer. The basic requirements of the communication system are:

Commands and telemetry between SWISH spectrometer and the PC include:

a. Sample rates
b. Integration periods
c. Photo array bias voltages, sensitivity and temperature
d. FPGA mode, clock, spectral analysis and sum/average parameters

Coefficients sent to the instrument for onboard spectral analysis will include:

a. Dark current & sensitivity correction on a pixel by pixel basis
b. Inter-pixel spillage correction
c. Data re-ordering from pixel indexing to waveguide indexing
d. Waveguide pair common and differential mode gain correction
e. Time domain windowing to reduce frequency leakage

f. Discrete cosine transform

g. Waveguide pair differential delay error corrections.

Housekeeping and status from the SWISH spectrometer will report on:

a. Photo array temperature

b. Power supply rail voltages and

c. FPGA mode, clock, spectral analysis and sum/average status

The above requirements were taken from Robertson and Scott (2010b).

9.3.4 Design

9.3.4.1 Interface

Communication from the host PC to the SWISH spectrometer is implemented through a USB interface. The USB interface is used to download commands and parameters to the FPGA and to upload house keeping and status telemetry to the host computer. The USB interface chip, FT2232D, manufactured by Future Technology is used. Future Technology provides documentation for the FT2232D that identifies communication structure from a PC through the USB interface to the FT2232D chip.

9.3.4.2 Data Format

The maximum number of bytes in a command/telemetry packet is 512. All ports are configured to operate in byte wide First In First Out (FIFO) mode. Port A has been defined as the command port

and Port B the telemetry port. Each packet is transferred from least significant to most significant byte (Robertson and Scott, 2010b).

9.3.4.3 Sending Commands

The structure of a command is 14 bytes and, if necessary, a specified number of bytes containing data added. Commands are used to switch modes of the spectrometer as well as read and write to memory onboard the spectrometer. A command specifying a mode switch is 14 bytes long with the least significant 3 bytes of the command/telemetry specification word set to a non zero value. A command requesting read access to memory is 14 bytes long specifying a start address and a byte count. The acknowledge command will return the standard 14 bytes plus the byte count of memory data. A command prompting the electronics to write to memory will contain 14 bytes including a start address, byte count, and a byte count number of data bytes. The data bytes will be written in order of received order beginning at the memory address. After a command is sent, acknowledge telemetry that echoes the original command is returned (Robertson and Scott, 2010b).

9.3.4.4 Receiving Telemetry

When the spectrometer is in operating mode, a single frame of data consists of 1100 bytes split into 3 packets. Each packet contains 4 frame sync bytes, a sequence count and a checksum. The first packet contains housekeeping data and has a length of 48 bytes. This includes the temperature of the detector, waveguide, frame averaging count and a timestamp. The second and third packets each contain a half of the detectors photo array and are each 512 bytes in length (Robertson and Scott, 2010b).

9.3.4.5 Programming Language

Communication to the FTDI USB chip is implemented through a driver written in C code. The host PC GUI is implemented with Matlab. The GUI interacts with the spectrometer using wrapper functions allowing the Matlab code to effectively call the C driver functions.

9.3.4.6 Communication Structure

There are two types of transactions that occur between the computer software and the SWSH instrument, command-acknowledge transaction and spectral or raw data telemetry transactions. The command-acknowledge transaction is used to read and write data to the instrument, while and spectral or raw data telemetry transactions are used to read data from the instrument.

When in quiescent mode, the SWISH spectrometer is not collecting or sending data. It responds to commands with either an acknowledge telemetry packet or, if requested, an acknowledge telemetry packet with memory data. The host PC is only able to write to memory within the SWISH spectrometer while it is operating in quiescent mode.

When in operating mode, the SWISH spectrometer is streaming data to the FTDI buffer where it is stored until the host PC reads it. The data contains housekeeping data as well as the sums of the pixels over a specified number of frames read from the photo array.

An overview of the communication and data handling between all of the components is shown in the flow diagram below:

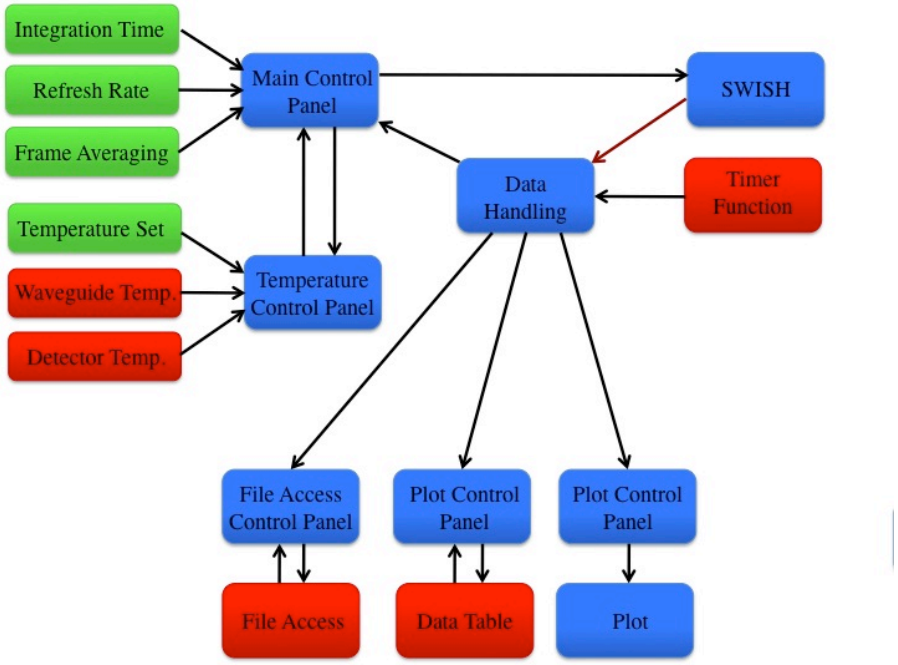

Figure 42: Overview of communication and data handling within the host computer.

The operation of beginning to collect data with the spectrometer begins with first sending a command to switch the spectrometer into quiescent mode, regardless of its current state. A series of commands are then sent writing to memory space in the spectrometer detailing user-chosen parameters. After each command is sent, telemetry is received confirming that the memory addresses was successfully written to. Once all parameters are uploaded to the spectrometer, a command is sent changing the mode into operational. The spectrometer then begins streaming data to the buffer where it is acquired by the user interface. The structure of a send/receive command is shown below.

a.

Frame Sync	Sequence Count	256 Bytes of Pixel Data	Checksum

b.

Frame Sync	Detector Temperature	Waveguide Temperature	Sequence Count	Checksum

c.

Frame Sync	Command/Telemetry Specification	Command Status	Start Address	Word/Sequence Count	Data Parameters (optional)	Checksum

Figure 43: (a) Standard streaming packet header (b) Standard streaming packet (c) Standard send command/receive acknowledgement command

The sampling frequency and integration periods are controlled by setting coefficients that drive biases to the photo array. LSync is the input signal to the detector which when high, dictates the array begin integration and when switched to low, dictates the stop of integration and begins reading out pixel data (Robertson et. al., 2010a).

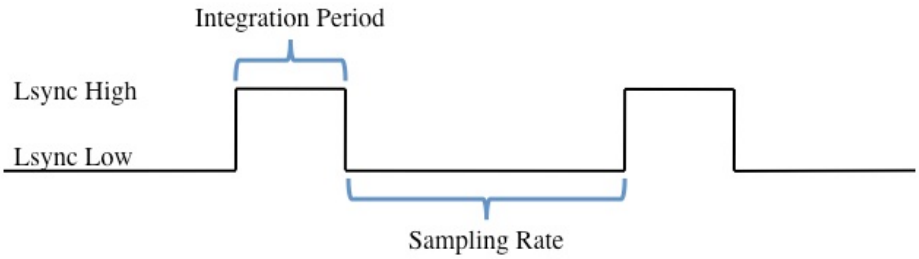

Figure 44: An illustration showing how the LSync line is used to control the integration period and sampling rate of the detector.

The sampling frequency represents the time between integration periods of the detector single. This frequency is what largely determines the data rate from the spectrometer. It is measured in detector clock cycles which, with the detector running at 24 MHz, has corresponding values shown in the table below. The clock cycle number is the value uploaded to the spectrometer to set the sampling frequency.

Table 6: Select sample frequency and integration period values.

Clock Cycles	Sampling Frequency	Clock Cycles	Integration Period
1.2766e+10	0.1s	6.3829e+04	0.5µs
3.1915e+10	0.25s	1.2766e+05	1 µs
6.3830e+10	0.5 s	2.5532e+05	2 µs
9.5745e+10	0.75 s	6.3830e+05	5 µs
1.2766e+11	1 s	1.2766e+06	10 µs
2.5532e+11	2 s	6.3830e+06	50 µs
3.8298e+11	3 s	1.2766e+07	100 µs

The integration period is also measured in detector clock cycles. Several values pre-programmed into the user interface are shown above. A timer function within the user interface is set to operate at the refresh rate equal to the spectrometer. Each time the timer function is called, the buffer is read out, data is extracted and begins a processing cycle. Frame averaging commands the spectrometer to

add a subsequent number of frames, passing the summation of the frames to the buffer. This can be used to lower the data rate of the spectrometer.

Several techniques are used to verify the validity of data. These included methods for searching for frame sync words within the captured frame to authenticate correct packet length. A data sequence count, incremented for every packet sent from the spectrometer, will further help ensure the two packets containing pixel data are obtained.

9.4 APPENDIX D: Waveguide Map

Port #	Mon or MZI port	Structure	Monitor or MZI #	Monitor Length or MZI Delay
1	Throughport	Monitor	1	76080.167
2	Throughport	Monitor	2	76142.212
3	Throughport	MZI	2	216.181
4	Crossport	MZI	2	216.181
5	Crossport	MZI	1	108.091
6	Throughport	MZI	1	108.091
7	Throughport	MZI	4	432.362
8	Crossport	MZI	4	432.362
9	Crossport	MZI	3	324.272
10	Throughport	MZI	3	324.272
11	Throughport	MZI	6	648.543
12	Crossport	MZI	6	648.543
13	Crossport	MZI	5	540.453
14	Throughport	MZI	5	540.453
15	Throughport	MZI	8	864.725
16	Crossport	MZI	8	864.725
17	Crossport	MZI	7	756.634
18	Throughport	MZI	7	756.634
19	Throughport	MZI	10	1080.906
20	Crossport	MZI	10	1080.906
21	Crossport	MZI	9	972.815
22	Throughport	MZI	9	972.815
23	Throughport	MZI	12	1297.087
24	Crossport	MZI	12	1297.087
25	Crossport	MZI	11	1188.996
26	Throughport	MZI	11	1188.996
27	Throughport	Monitor	3	74576.206

28	Throughport	MZI	14	1513.268
29	Crossport	MZI	14	1513.268
30	Crossport	MZI	13	1405.178
31	Throughport	MZI	13	1405.178
32	Throughport	MZI	16	1729.449
33	Crossport	MZI	16	1729.449
34	Crossport	MZI	15	1621.359
35	Throughport	MZI	15	1621.359
36	Throughport	MZI	18	1945.630
37	Crossport	MZI	18	1945.630
38	Crossport	MZI	17	1837.540
39	Throughport	MZI	17	1837.540
40	Throughport	MZI	20	2161.812
41	Crossport	MZI	20	2161.812
42	Crossport	MZI	19	2053.721
43	Throughport	MZI	19	2053.721
44	Throughport	MZI	22	2377.993
45	Crossport	MZI	22	2377.993
46	Crossport	MZI	21	2269.902
47	Throughport	MZI	21	2269.902
48	Throughport	MZI	24	2594.174
49	Crossport	MZI	24	2594.174
50	Crossport	MZI	23	2486.083
51	Throughport	MZI	23	2486.083
52	Throughport	Monitor	4	72350.458
53	throughport	MZI	26	2810.355
54	Crossport	MZI	26	2810.355
55	Crossport	MZI	25	2702.265
56	Throughport	MZI	25	2702.265
57	Throughport	MZI	28	3026.536
58	Crossport	MZI	28	3026.536
59	Crossport	MZI	27	2918.446
60	Throughport	MZI	27	2918.446
61	Throughport	MZI	30	3242.717
62	Crossport	MZI	30	3242.717
63	Crossport	MZI	29	3134.627
64	Throughport	MZI	29	3134.627
65	Throughport	MZI	32	3458.899
66	Crossport	MZI	32	3458.899
67	Crossport	MZI	31	3350.808
68	Throughport	MZI	31	3350.808
69	Throughport	MZI	34	3675.080
70	Crossport	MZI	34	3675.080
71	Crossport	MZI	33	3566.989
72	Throughport	MZI	33	3566.989
73	Throughport	MZI	36	3891.261
74	Crossport	MZI	36	3891.261

75	Crossport	MZI	35	3783.170
76	Throughport	MZI	35	3783.170
77	Throughport	Monitor	5	70252.731
78	Throughport	MZI	38	4107.442
79	Crossport	MZI	38	4107.442
80	Crossport	MZI	37	3999.351
81	Throughport	MZI	37	3999.351
82	Throughport	MZI	40	4323.623
83	Crossport	MZI	40	4323.623
84	Crossport	MZI	39	4215.533
85	Throughport	MZI	39	4215.533
86	Throughport	MZI	42	4539.804
87	Crossport	MZI	42	4539.804
88	Crossport	MZI	41	4431.714
89	Throughport	MZI	41	4431.714
90	Throughport	MZI	44	4755.986
91	Crossport	MZI	44	4755.986
92	Crossport	MZI	43	4647.895
93	Throughport	MZI	43	4647.895
94	Throughport	MZI	46	4972.167
95	Crossport	MZI	46	4972.167
96	Crossport	MZI	45	4864.076
97	Throughport	MZI	45	4864.076
98	Throughport	MZI	48	5188.348
99	Crossport	MZI	48	5188.348
100	Crossport	MZI	47	5080.257
101	Throughport	MZI	47	5080.257
102	Throughport	MZI	50	5404.529
103	Crossport	MZI	50	5404.529
104	Crossport	MZI	49	5296.438
105	Throughport	MZI	49	5296.438
106	Throughport	MZI	52	5620.710
107	Crossport	MZI	52	5620.710
108	Crossport	MZI	51	5512.620
109	Throughport	MZI	51	5512.620
110	Throughport	Monitor	6	72381.197
111	Throughport	MZI	54	5836.891
112	Crossport	MZI	54	5836.891
113	Crossport	MZI	53	5728.801
114	Throughport	MZI	53	5728.801
115	Throughport	MZI	56	6053.073
116	Crossport	MZI	56	6053.073
117	Crossport	MZI	55	5944.982
118	Throughport	MZI	55	5944.982
119	Throughport	MZI	58	6269.254
120	Crossport	MZI	58	6269.254
121	Crossport	MZI	57	6161.163

122	Throughport	MZI	57	6161.163
123	Throughport	MZI	60	6485.435
124	Crossport	MZI	60	6485.435
125	Crossport	MZI	59	6377.344
126	Throughport	MZI	59	6377.344
127	Throughport	MZI	62	6701.616
128	Crossport	MZI	62	6701.616
129	Crossport	MZI	61	6593.525
130	Throughport	MZI	61	6593.525
131	Throughport	MZI	64	6917.797
132	Crossport	MZI	64	6917.797
133	Crossport	MZI	63	6809.707
134	Throughport	MZI	63	6809.707
135	Throughport	MZI	66	7133.978
136	Crossport	MZI	66	7133.978
137	Crossport	MZI	65	7025.888
138	Throughport	MZI	65	7025.888
139	Throughport	MZI	68	7350.160
140	Crossport	MZI	68	7350.160
141	Crossport	MZI	67	7242.069
142	Throughport	MZI	67	7242.069
143	Throughport	Monitor	7	75365.442
144	Throughport	MZI	70	7566.341
145	Crossport	MZI	70	7566.341
146	Crossport	MZI	69	7458.250
147	Throughport	MZI	69	7458.250
148	Throughport	MZI	72	7782.522
149	Crossport	MZI	72	7782.522
150	Crossport	MZI	71	7674.431
151	Throughport	MZI	71	7674.431
152	Throughport	MZI	74	7998.703
153	Crossport	MZI	74	7998.703
154	Crossport	MZI	73	7890.612
155	Throughport	MZI	73	7890.612
156	Throughport	MZI	76	8214.884
157	Crossport	MZI	76	8214.884
158	Crossport	MZI	75	8106.794
159	Throughport	MZI	75	8106.794
160	Throughport	MZI	78	8431.065
161	Crossport	MZI	78	8431.065
162	Crossport	MZI	77	8322.975
163	Throughport	MZI	77	8322.975
164	Throughport	MZI	80	8647.246
165	Crossport	MZI	80	8647.246
166	Crossport	MZI	79	8539.156
167	Throughport	MZI	79	8539.156
168	Throughport	MZI	82	8863.428

169	Crossport	MZI	82	8863.428
170	Crossport	MZI	81	8755.337
171	Throughport	MZI	81	8755.337
172	Throughport	MZI	84	9079.609
173	Crossport	MZI	84	9079.609
174	Crossport	MZI	83	8971.518
175	Throughport	MZI	83	8971.518
176	Throughport	Monitor	8	86203.071
177	Throughport	MZI	86	9295.790
178	Crossport	MZI	86	9295.790
179	Crossport	MZI	85	9187.699
180	Throughport	MZI	85	9187.699
181	Throughport	MZI	88	9511.971
182	Crossport	MZI	88	9511.971
183	Crossport	MZI	87	9403.881
184	Throughport	MZI	87	9403.881
185	Throughport	MZI	90	9728.152
186	Crossport	MZI	90	9728.152
187	Crossport	MZI	89	9620.062
188	Throughport	MZI	89	9620.062
189	Throughport	MZI	92	9944.333
190	Crossport	MZI	92	9944.333
191	Crossport	MZI	91	9836.243
192	Throughport	MZI	91	9836.243
193	Throughport	MZI	94	10160.515
194	Crossport	MZI	94	10160.515
195	Crossport	MZI	93	10052.424
196	Throughport	MZI	93	10052.424
197	Throughport	MZI	96	10376.696
198	Crossport	MZI	96	10376.696
199	Crossport	MZI	95	10268.605
200	Throughport	MZI	95	10268.605
201	Throughport	MZI	98	10592.877
202	Crossport	MZI	98	10592.877
203	Crossport	MZI	97	10484.786
204	Throughport	MZI	97	10484.786
205	Throughport	MZI	100	10809.058
206	Crossport	MZI	100	10809.058
207	Crossport	MZI	99	10700.968
208	Throughport	MZI	99	10700.968
209	Throughport	Monitor	9	98869.299
210	Throughport	Monitor	10	98926.591
211	Throughport	Monitor	11	98984.178

9.5 Appendix E: Satellite Observations of Water Vapor

9.5.1 Instruments that have made Water Vapor Measurements:

Instrument	View	Weight	Size	Power	Swath	Spectral Bands	Spectral Resolution
HALOE	Solar Occultation (15~60-130km)	101kg	36in			2.5-11um	
ACE-FTS	Solar Occultation	41kg		37W	1.25mrad (FOV)	2.2-13.3um	$0.02cm^{-1}$
MAESTRO	Solar Occultation (10-100km)	8kg				285-1030nm	1-2nm
MODIS	Nadir	228.7kg	1*1*1.6m	162.5W	2330*10 km	0.4-14.4um	
GOMOS	limb					0.25-0.95nm	
MIPAS	limb				3*30km	4.15-14.6um	0.035lines/cm
TES	nadir and limb	385kg	1*1.3*1.4	334W	2.3*23limb	3.2-15.4um	$0.00025cm^{-1}$
SAGE III	solar occultaton	76kg	73*45*93cm	80W		0.29-1.03um	1-2nm
POAM III	solar occultaton					353.4-1018nm	
MISR	nadir	148kg		117W	9 cameras	4 bands at 446, 558, 672, and 867	
MAS	limb						
SCIAMCHY	nadir/limb+ occultation	198kg		122W	limb 3*132km	(240 nm - 2380 nm	0.2-0.5

9.5.2 Characterization of Instruments:

Instrument	View	Weight	Size	Power	Swath	Spectral Bands	Spectral Resolution
HALOE	Solar Occultation	101kg	36in			2.5-11um	

	(15~60-130km)						
ACE-FTS	Solar Occultation	41kg		37W	1.25mrad (FOV)	2.2-13.3um	0.02cm^{-1}
MAESTRO	Solar Occultation (10-100km)	8kg				285-1030nm	1-2nm
MODIS	Nadir	228.7kg	1*1*1.6m	162.5W	2330*10 km	0.4-14.4um	
GOMOS	limb					0.25-0.95nm	
MIPAS	limb				3*30km	4.15-14.6um	0.035lines/cm
TES	nadir and limb	385kg	1*1.3*1.4	334W	2.3*23limb	3.2-15.4um	0.00025cm^{-1}
SAGE III	solar occultaton	76kg	73*45*93cm	80W		0.29-1.03um	1-2nm
POAM III	solar occultaton					353.4-1018nm	
MISR	nadir	148kg		117W	9 cameras	4 bands at 446, 558, 672, and 867	
MAS	limb						
SCIAMCHY	nadir/limb+ occultation	198kg		122W	limb 3*132km	(240 nm - 2380 nm	0.2-0.5

9.6 Appendix F: Communication Structure

Command-Acknowledge Transactions

The following was taken from Robertson et. al. (2011). The SWSH FPGA will accept all command packet data/parameters as valid even if the checksum is incorrect.

On receiving a command packet the FPGA will respond with an acknowledge telemetry packet with optional data, command checksum status and other status. These acknowledge will be delayed if a Spectral/Raw Data telemetry transaction is in progress.

There are only three types of Command-Acknowledge transactions that will be used as shown below.

Command Telemetry Word 2 Bits 15..14	Command	Telemetry
00	No use anticipated Packet Length = 6 words	No use anticipated Packet Length = 6 words
01	The command supplies: 1. A "Start address" and 2. A "word count" No data is supplied. Note: Number of words = "word count"+1 The command requests that data is: read from the memory (register) map space from "Start address" to ("Start address" + "word count" – 1) and the read data be returned with the acknowledge telemetry packet. Packet Length = 6 words	The acknowledge telemetry packet contains: 1. A "Start address" 2. A "word count" 3. "word count" words of data and 4. Basic Status Note: Number of words = "word count"+1 The "Start address" and "word count" are those supplied by the command. The "words of data" is that read from the memory (register) map space from "Start address" to ("Start address" + "word count") Packet Length = "word count" + 7 words
10	The command supplies: 1. A "Start address" 2. A "word count" and 3. "word count" words of data. Note: Number of words = "word count"+1 The command requests that The data is written to the memory (register) map space from "Start address" to ("Start address" + "word count" – 1)	The acknowledge telemetry packet contains only the basic status information.

	and only basic status be returned in the acknowledge telemetry packet. Packet Length = "word count" + 7 words	Packet Length = 6 words
11	This command supplies data to be written as "10" above. Upon completion the data is immediately read back and telemetered as in "01" above. Packet Length = "word count" + 7 words	Data is read back and telemetered as in "01" above. Packet Length = "word count" + 7 words

Table 7 Three used Command-Acknowledge transactions